

MOLECULAR DYNAMICS SIMULATION STUDY OF SOLID-LIQUID INTERFACE  
PROPERTIES OF HCP MAGNESIUM

MOLECULAR DYNAMICS SIMULATION STUDY OF SOLID-LIQUID INTERFACE  
PROPERTIES OF HCP MAGNESIUM

By

YUNFEI BAI, B. Eng.

A Thesis

Submitted to the School of Graduate Studies  
in Partial Fulfillment of the Requirements  
for the Degree of  
Master of Applied Science

McMaster University

© Copyright by Yunfei Bai, September 2012

MASTER OF APPLIED SCIENCE (2012)

McMaster University

(Materials Science and Engineering)

Hamilton, Ontario

TITLE: Molecular dynamics simulation study of solid-liquid  
interface properties of HCP magnesium

AUTHOR: Yunfei Bai, B. Eng.  
(University of Science and Technology Beijing)

SUPERVISOR: Dr. Jeffrey J. Hoyt

NUMBER OF PAGES: xvi, 74

## Abstract

The structural and thermodynamic properties of a crystal-melt interface in elemental magnesium have been investigated using molecular dynamics (MD) simulations with an embedded atom method description of the interatomic potential. Three low index interfacial orientations, (0001),  $(1\bar{1}01)$  and  $(11\bar{2}0)$ , have been studied. From fine-grained atomic density profiles, the structural interfacial widths show obvious anisotropy and the variation of interatomic planar spacing as a function of distance through the crystal-melt boundary is established. Mainly from the coarse-grained density profiles, the effective 10-90 width of the interface region, defined as the intrinsic width, in each orientation has been determined. In addition, the interfacial stresses are obtained from an integration of the interfacial stress profiles and the results show significant anisotropy, which is possibly related to the anisotropy of occupation fraction profiles. Finally, from a determination of the excess energy and interfacial stress of the solid-liquid interface and from previous published results for the interfacial free energy at the melting point, the Gibbs-Cahn integration is employed to derive an estimation of the temperature dependence of the interfacial free energy at non-equilibrium temperatures. All of the crystal-melt interfacial properties for magnesium are compared with simulation data from other elemental metals and alloys, as well as from other model systems such as Lennard-Jones and hard spheres.

## **Acknowledgement**

YFB would like to express his deepest gratitude and respect to his supervisor Dr. Jeffrey J. Hoyt for his inspirational guidance, treasured advice and motivational instructions to this research work. I am appreciative to Dr. Hoyt for introducing this atomistic simulation research area to me and guiding me through programing and thermodynamic knowledge. It is also a life-time valuable experience for me to improve my skills of learning and problem solving.

This research work is financially supported by the Magnesium Network (MagNET) under the Natural Sciences and Engineering Research Council of Canada (NSERC). The author is also pleased to thank the Shared Hierarchical Academic Research Computing Network (SHARCNET) for providing such high performance computing resources to perform this research.

This research work would not have been possible without the support from Dr. Hoyt, Dr. Nikolas Provatas and all the members from computational material science group for sharing experience and valuable resources. The author would also like to convey thanks to the staff, faculty and fellow students of department of Material Science and Engineering, McMaster University for their great support and company.

Last but not least, I wish to express my love and gratitude to my beloved parents and sister, for their understanding, care and endless support through the duration of my studies.

# Table of Contents

<b>Abstract.....</b>	<b>iii</b>
<b>Acknowledgement.....</b>	<b>iv</b>
<b>Table of Contents.....</b>	<b>vi</b>
<b>List of Figures.....</b>	<b>ix</b>
<b>List of Tables.....</b>	<b>xi</b>
<b>List of Symbols.....</b>	<b>xii</b>
<b>1 INTRODUCTION.....</b>	<b>1</b>
1.1 Why Magnesium: Background.....	2
1.2 MD Simulation of Mg: Motivation.....	2
1.2.1 Interfacial Structure.....	2
1.2.2 Temperature Dependence of $\gamma$ at Non-equilibrium Temperatures...	3
1.3 MD Simulation of Mg: Research Objectives.....	4
1.4 Thesis Outline.....	5
<b>2 GENERAL THEORY.....</b>	<b>6</b>
2.1 Molecular Dynamics Simulations.....	6

2.1.1 Potentials.....	9
2.1.2 Ensembles.....	15
2.1.3 Simulation Box in the Simulation Process.....	17
2.2 Structural Characterization of Solid-Liquid Interface.....	18
2.2.1 Fine-grained Density.....	19
2.2.2 Coarse-grained Density.....	21
2.2.3 Layer Separation.....	23
2.2.4 Interface Stress Profile.....	24
2.3 Interfacial Free Energy $\gamma$ .....	25
2.3.1 Previous Research.....	26
2.3.1.1 Experimental Measurement.....	26
2.3.1.2 Anisotropy and its Experimental Measurement.....	28
2.3.1.3 Temperature Dependence of $\gamma$ .....	29
2.3.2 Thermodynamic Integration Technique.....	31
<b>3 SIMULATION PROCESS.....</b>	<b>36</b>
3.1 Melting Temperature.....	36
3.2 Equilibration of Crystal-Melt Model.....	37
3.3 Obtain Data.....	37
<b>4 RESULTS, ANALYSIS AND DISCUSSION.....</b>	<b>39</b>
4. 1 Structure.....	39

4.1.1 Interfacial Widths.....	40
4.1.1.1 Structural Widths.....	44
4.1.1.2 Intrinsic Widths.....	45
4.1.1.3 Interfacial Widths from Other Interfacial Profiles.....	46
4.1.2 Layer Separation.....	47
4.1.3 Stress Profiles and Their Anisotropy.....	50
4.2 Temperature Dependence of $\gamma$ at Non-equilibrium Temperatures.....	56
<b>5 FUTURE RESEARCH.....</b>	<b>62</b>
<b>6 CONCLUSION.....</b>	<b>64</b>
<b>References.....</b>	<b>67</b>

## List of Figures

Figure 2.1	A Simple flow chart of Molecular dynamics simulation.....	8
Figure 2.2	Lennard-Jones potential, attraction and repulsive contribution and WCA model.....	11
Figure 2.3	Logarithm $S$ versus $\varepsilon$ for (0001) orientation illustrating the procedure for determining optimal values in the FIR filter function.....	22
Figure 2.4	Diagram of the molar volume $v$ and molar entropy $s$ across the interface.....	30
Figure 4.1	Fine-grained density profile (a) and coarse-grained density profile (b) of the (0001) crystal-melt interface as a function of $z$ direction, a direction perpendicular to the studied interface.....	40
Figure 4.2	Fine (a) and coarse-grained (b) density profiles of the $(1\bar{1}01)$ interface along the vertical direction of the interface studied.....	41
Figure 4.3	Fine and coarse-grained density profiles of the $(11\bar{2}0)$ interface along $z$ direction.....	42
Figure 4.4	Potential energy density profiles for the three interfaces as a function of a variety of positions through $z$ direction.....	43

Figure 4.5	The interplane spacing as a function of distance normal to the interface for the FCC (100), (110), and (111) LJ solid-liquid interfaces in LJ reduced unit.....	48
Figure 4.6	Layer spacing variations with the direction along interface normal for three interfaces.....	49
Figure 4.7	Interfacial stress profiles along the interface normal for all three directions.....	51
Figure 4.8	Interfacial stress profiles for the LJ crystal-melt interface at equilibrium temperature for (111), (100) and (111) interfaces.....	52
Figure 4.9	Occupation fraction profiles $N_i/N_c$ along $z$ direction for all three interfaces.....	54
Figure 4.10	Occupation fraction, $N_i/N_c$ , as function of position for three interfaces across the solid-liquid interface with Lennard Jones potential at its equilibrium temperature .....	55
Figure 4.11	The $d[(\rho^{-2/3}Y)/T]/dT$ , varying with temperature for all three interfaces. The total values and the partial values contributed by excess energy $e$ are plotted respectively.....	58
Figure 4.12	Temperature dependence of $\gamma$ for the three interfaces under non-equilibrium temperatures until the melting point $T_M$ .....	60

## List of Tables

Table 4.1	Interfacial widths from various types of profiles of the three different interface.....	43
Table 4.2	Excess energy $e$ , interfacial stress $\tau$ and excess entropy $\eta$ calculated at melting temperature.....	57
Table 4.3	Bulk solid density at chosen temperature and bulk solid and liquid number and energy densities at $T_M$ .....	57
Table 4.4	$\gamma$ under non-equilibrium condition at selected temperatures.....	59

## List of Symbols

$\gamma$	Interfacial free energy
$\tau$	Interfacial stress
$\vec{F}_i$	Force vector exerted on the atom $i$
$i$	A specific atom
$m_i$	Mass of atom $i$
$v_i$	Velocity of atom $i$
$k_B$	Boltzmann coefficient
$K_E$	Total kinetic energy of a system
$\vec{a}_i$	Acceleration vector of atom $i$
$r$	Absolute value of coordinate vector
$\vec{r}_i$	Coordinate vector for atom $i$
$U(\vec{r}_i)$	Intermolecular potential in terms of coordinate vector
$\Delta t$	Minimum time interval (timestep)
$\sigma$	Length that the potential of a pair is zero (cutoff distance)
$\varepsilon$	Depth of potential well, a real number
$\phi(r_{ij})$	Host lattice relaxation (pair potential function)
$E_i(r)$	Potential energy of an atom $i$

$\rho(r_{ij})$	Electron density function
$F(\sum_{i \neq j} \rho(r_{ij}))$	Embedded energy term
$T^{hcp \rightarrow bcc}$	Transformation temperature from HCP to BCC structures
$T$	Temperature
$P$	Pressure
$N$	Number of particles of a system
$X$	Representative point of phase space
$\Lambda$	Phase space
$p_i$	State probability function
$\langle f \rangle$	Average value of a macroscopic property
$V$	Volume
$E$	Internal energy
$\mu$	Chemical potential or interface mobility
$H$	Enthalpy
$a$	Lattice constant in the HCP
$c$	Lattice constant in the HCP
$x$	One coordinate direction parallel to the interface
$y$	The other coordinate direction parallel to the interface
$z$	Coordinate direction along interface normal
$N_z$	Number of atoms in a given $xy$ plane
$\Delta z$	Bin thickness along $z$ direction
$L_x$	Length of the system along the $x$ axis

$L_y$	Length of the system along the $y$ axis
$\phi$	Local order parameter
$\vec{r}_i^{hcp}$	Coordinate vector in perfect HCP structures
$\vec{f}_i$	The filtered value of the coarse scale type at position $i$
$w_k$	Filter coefficient of a Gaussian form:
$f_{i+k}$	Fine scale density value of neighbor $k$
$S$	Summed value in minimization process or entropy
$n$	A real number
$w_{10-90}$	10-90 width of interface region
$A$	Area of interface or a coefficient
$\delta_{ij}$	Kronecker symbol
$\sigma_{ij}$	Average stress tensor
$\varepsilon_{ij}$	Average strain tensor
$s$	Denote solid
$l$	Denote liquid
$V^s$	Volume of solid
$\mu_m$	Chemical potential of a specie $m$
$N_m$	Number of a specie $m$
$G$	Gibbs free energy
$G_{bulk}$	Gibbs free energy of bulk
$N_A$	Avogadro's number

$\alpha$	Turnbull coefficient and phase superscripts
$\Delta H_{fus}$	Molar latent heat of fusion
$\beta$	Phase superscripts
$S_{ex}$	Excess interfacial entropy
$V_{ex}$	Excess volume
$s$	Molar entropy
$v$	Molar volume
$v'$	Dendritic tip velocity
$r'$	Dendritic tip radius
$V^l$	Volume of liquid
$S^s$	Entropy of solid
$S^l$	Entropy of liquid
$N^s$	Number particle of solid
$N^l$	Number particle of liquid
$A$	Interface area
$e$	Excess internal energy
$\rho_s$	Number density of bulk solid
$\rho_l$	Number density of bulk liquid
$\rho_s^E$	Energy density of bulk solid
$\rho_l^E$	Energy density of bulk liquid
$K$	Constant coefficient in expression of density

$L_s$	Length of bulk solid in system according to Gibbs dividing surface
$L_l$	Length of bulk liquid in system according to Gibbs dividing surface
$L$	Length of the system along interface normal
$T_M$	Melting temperature
$S(q)$	Liquid structure factor in density functional theory
$N_i$	Number of particles in a layer
$N_c$	Number of particles in a bulk crystal layer
$z^{peak}$	Position of peak value
$\rho$	Number density
$\eta$	Entropy of system
$v_{solid}$	Value of solid in a certain profile
$v_{liquid}$	Value of liquid in a certain profile

## **CHAPTER ONE**

### **INTRODUCTION**

---

The microscopic structural details and thermodynamic properties of the solid-liquid interface are always crucial factors in fully understanding many important phenomena such as nucleation, dendrite growth, liquid–metal embrittlement and wetting [1-4]. For decades, although many laboratory experiments have been performed with respect to estimates of the surface tension for limited kinds of systems [5-10], the properties of an interface between two condensed phases are difficult to determine experimentally [11] and especially the challenge is probing the interface at the atomic length scale [12]. These difficulties have spurred the development of atomistic simulation approaches, especially Molecular-Dynamics (MD) [13] and Monte-Carlo [14] methods, which can provide a link between structure and properties of interfaces. Elemental Magnesium with Hexagonal close-packed structure [15] is a very representative example and hasn't been fully investigated in terms of these properties. Thus it constitutes the subject of this thesis.

## **1.1 Why Magnesium: Background**

Magnesium is the eighth most abundant element in nature and the fourth most abundant metal in the earth's crust. Due to the low density, Mg and its alloys are good candidates for future applications in the aerospace and automotive industries. Since casting is one of the major methods of the manufacture of Mg materials, the crystal growth behavior in Mg during the solidification is an important factor in establishing the relationship between processing and properties. [15]

## **1.2 MD Simulation of Mg: Motivation**

### **1.2.1 Interfacial Structure**

With respect to computational modeling of Mg metal and alloys, some meaningful progress has been made, including the creation of an interatomic potential [16, 17], calculation of the crystal-melt interfacial free energy ( $\gamma$ ) [17] at the melting point and its anisotropy, the computation of the solid-liquid interface mobility ( $\mu$ ) [18, 19], simulation of mechanical properties [20, 21, 22] and modeling of solidification using the phase field method [23, 24]. However, far less attention has been paid to the atomic scale structure of the interface. Atomistic simulations have been used extensively to study structural properties of crystal-melt interfaces in BCC [25, 26, 27] and FCC [28-42] crystals and

considerable insight has been gained concerning the interface width, the variation of atomic plane spacing through the interface, the excess energy and the interface stress. On the other hand relatively little work [43, 44] has been devoted to the HCP system, and these structural and excess interface properties have not been determined in the case of Mg.

### **1.2.2 Temperature Dependence of $\gamma$ at Non-equilibrium Temperatures**

The interfacial free energy ( $\gamma$ ) is defined as the reversible work necessary to create a unit area of interface by Gibbs [45]. In the past decade it has been shown that  $\gamma$  of the solid-liquid interface, as well as its weak anisotropy, can be calculated quite precisely by two complementary MD methods: the cleaving method (CM), which was first proposed by Broughton and Gilmer [37] and then modified by Davidchack and Laird [46], and the capillary fluctuation method (CFM), first developed by Hoyt et al. [47]. Both of these two methods, however, require an equilibrium interface, that is, the computations are carried out at the melting temperature. From the practical standpoint of modeling the solidification of alloys, the temperature dependence of  $\gamma$  is required. In recent years, thermodynamic integration techniques have been employed to obtain  $\gamma$  as a function of temperature. In light of Cahn's extension [48] of Gibbs' formalism of interfacial thermodynamics [45], Frolov and Mishin first [49] applied the so-called 'Gibbs-Cahn integration' to the calculation of the temperature dependence of the surface free energy of solid Cu (110), and subsequently [50] the calculation of the solid-liquid interfacial free

energy of Cu-Ag along the temperature-composition curve in its phase diagram at a fixed pressure. It was then followed by Laird and Davidchack [41], who studied the temperature dependence of  $\gamma$  along the coexistence curve in the pure Lennard-Jones (LJ) system. All previous work on the temperature dependence of  $\gamma$  has been limited to BCC and FCC systems at the equilibrium condition. It is not clear what the situation will be like in the non-cubic crystal structures at a more practical non-equilibrium condition during solidification process. For the case of HCP Mg, Sun et al. [17] used the CFM to compute  $\gamma$  and described in detail how the anisotropy can be expressed in an HCP system, but the temperature dependence of the interfacial free energy has not been investigated.

### **1.3 MD Simulation of Mg: Research Objectives**

The purpose of the present MD study is two-fold. First, we will study the atomic structure of the solid-liquid interface of an HCP Mg using an embedded-atom method (EAM) description of the interatomic potential [16, 17]. Three low index orientations will be investigated: the basal plane (0001),  $(1\bar{1}01)$  and  $(11\bar{2}0)$  and characterization of the interface will involve multiple descriptions: fine and coarse density profiles, the potential energy profile, the stress profile, the 10-90 width of the interface and the layer separation. Each of these quantities will be described in detail in the next section. Second, we will apply ‘Gibbs-Cahn integration’ to all three orientations to obtain the temperature dependence of the interfacial free energy at non-equilibrium temperatures. The integration will be performed from a starting point of the value of  $\gamma$  at the melting

temperature previously determined in Ref. [17] and will utilize values of the excess internal energy  $e$  and interfacial stress  $\tau$ , which will be calculated in this work.

## 1.4 Thesis Outline

The outline of the thesis is as follows. We begin in Chapter two by introducing general theory about structural and thermodynamic characterizations of the interface as well as major concepts in MD simulations. In Chapter three we briefly describe the technical procedures in our MD simulations. All the results from simulation, their analysis and discussions are presented in Chapter four. Suggested future work is summarized in Chapter five and finally we conclude in Chapter six.

## **CHAPTER TWO**

### **GENERAL THEORY**

---

The general theory consists of three parts. First, the molecular dynamics simulation, which is the computational method employed in this whole investigation, is introduced with details as a basic background. In this part, potentials and several thermodynamic ensembles are explained as vital concepts in order to understand the way the molecular dynamics simulations perform. In the end of the first part, the information about the simulation box is introduced. Second, several characterization methods are generally applied to this simulation system to get enough information about structural details of solid-liquid interface. These structural characterization methods will be introduced in detail in the second part. Last but not least, previous research on interfacial free energy and a chosen thermodynamic integration technique, called ‘Gibbs-Cahn integration’ to calculate the temperature dependence of interfacial free energy will be described in the final part of this chapter.

### **2.1 Molecular Dynamics Simulations**

Crystal-melt interface of metals consists of several atomic layers. This microscopic structure cannot be easily studied by conventional experiments. Molecular

dynamics simulation is the method that dynamically investigates a group of atoms with their positions and velocities evolving with time and can be related to macroscopic properties such as temperature and pressure. In other words, molecular dynamics simulation is the method that computationally helps to build a bridge between the microscopic structure that we can barely measure and macroscopic properties with which we can usually describe the tangible world. Following is the simplified description of how the molecular dynamics simulation works.

Molecular dynamics simulation is essentially the solution of Newton's second law or the equation of motion, which for a simple system of atoms, where a specific atom to be studied is denoted as atom  $i$ , can be expressed as

$$\vec{F}_i = m_i \vec{a}_i \quad (2.1)$$

and

$$\vec{F}_i = -\nabla U(\vec{r}_i) \quad (2.2)$$

where the  $\vec{F}_i$  denotes the force exerted on the atom  $i$  by all atoms in the system except for itself. And  $m_i$  and  $\vec{a}_i$  are the mass and acceleration vector of that atom respectively. As in the equation 2.2, the force can be calculated by the first derivative of an intermolecular potential  $U(\vec{r}_i)$  with respect to the coordinate vector  $\vec{r}_i$ . And more information about the intermolecular potential will be introduced in the second part of this chapter.

As described in Fig. 2.1, with intermolecular potential prepared, position and velocity of each atom are ready to be acquired by the integration of the equation of motion. Once original position and velocity of each atom of a system initialized, a code that contains a chosen algorithm can be applied to perform the calculation step-by-step

evolving the system with time as long as one need, under desired constrains defined by particular statistical ensembles, which will be introduced in the third part of molecular dynamic simulation. Details of algorithms will not be discussed here. Information about it can be referred to other references [51].

Relevant phase variables such as averaged temperatures and pressures can be calculated from updated coordinates and velocities of atoms by statistical physics. For example, in order to obtain the average temperature  $T$  from a three-dimensional system with the number atoms of  $N$ , the relation can be utilized [68]:

$$K_E = \sum_{i=1}^N \frac{1}{2} m_i v_i^2 = \frac{3}{2} N k_B T \quad (2.3)$$

where  $K_E$  is the total kinetic energy of  $N$  atoms,  $m_i$  and  $v_i$  are the mass and velocity respectively for an atom  $i$ , and  $k_B$  is the Boltzmann coefficient. Thus the average temperature and pressure can be related to the microscopic properties. These phase variables together with the positions of atoms could be stored at each time step for the analysis afterwards.

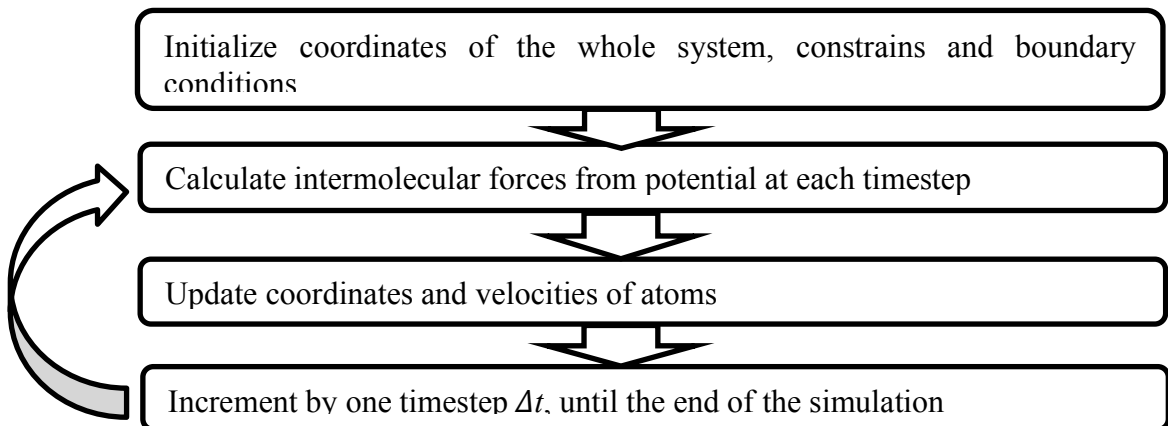


Fig. 2.1: A Simple flow chart of Molecular dynamics simulation

### 2.1.1 Potentials

As introduced previously, the intermolecular potential is a prerequisite of molecular dynamics simulations in order to calculate the forces exerted on atoms. The accuracy of simulation also largely relies on the accuracy of potential energy of the atoms. Thus the potential energy represents a very important factor in the MD simulation process.

An intermolecular potential is the potential energy describing interactions among the atoms. Development of potentials involves both the effects of attraction and repulsion of particles and theoretically it can be accurately calculated from first principle or ab initio approach [52]. However, it is only applicable for very simple systems. Commonly, some approximations have to be made to improve computational efficiency and it can be calibrated to experimental data, such as elastic modulus, melting temperature and structure coefficients, etc., to improve accuracy of the potential. Currently, many developed intermolecular potentials [52] provide a relatively good compromise between accuracy and computational efficiency. Among them, the Lennard-Jones potential is undoubtedly the most widely used potential in the last few decades. Thus the Lennard-Jones potential, most commonly used continuous pairwise potential, is a good start to get more familiar with the intermolecular potentials.

Lennard-Jones potential, also referred to as L-J potential or 6-12 potential, is a mathematical model for neutral atoms or molecules and was first introduced by John

Lennard-Jones in 1924 [53]. The most commonly used form of Lennard-Jones potential is

$$V_{LJ}(r) = 4\epsilon \left[ \left( \frac{\sigma}{r} \right)^{12} - \left( \frac{\sigma}{r} \right)^6 \right] \quad (2.4)$$

where  $\sigma$  is the length that the potential of a pair of atoms is zero,  $r$  is the length of the vector between two particles and  $\epsilon$  is the depth of the potential well. In some applications, the attractive interaction can be ignored compared with short-range repulsion. In that case, L-J potential is simplified by being truncated at the bottom of potential and then shifted upwards by well depth  $\epsilon$ , to give value of zero to the potential after the minimum position. The modification is called WCA model [54]. In Fig. 2.2, the lower smooth solid line is the L-J potential, where the minimum value  $-\epsilon$ , the well depth, exists at the position of  $r=2^{1/6} \sigma$ . The upper solid line represents truncated WCA model where the value at position  $r=2^{1/6} \sigma$  is shifted upwards to zero. The upper dotted line, with mathematical form of  $r^{-12}$ , characterizes the repulsive contribution and the lower one, with mathematical form of  $-r^{-6}$ , represents the attractive contribution to original L-J potential. As will be introduced in this thesis, there are many previous MD simulation results of structure properties with this the L-J potential, and some important results will be compared with our simulation results.

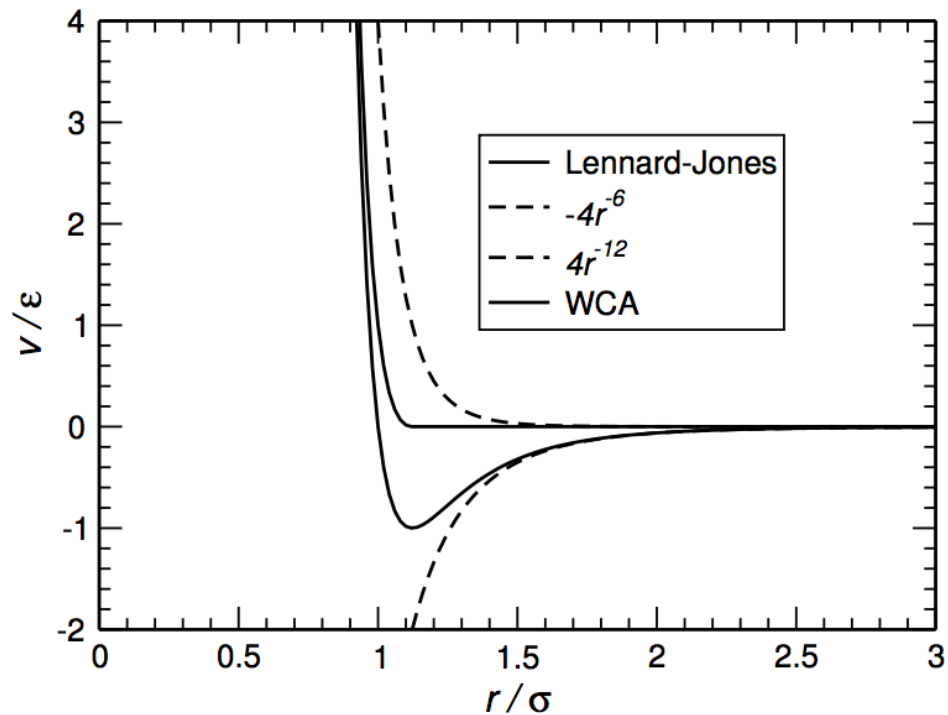


Fig. 2.2: Lennard-Jones potential, attraction and repulsive contribution and WCA model.

[55]

Although the Lennard-Jones potential works well in many applications in terms of bulks of metals, there is inaccuracy in this potential calculation in terms of impurities, surfaces and other defects [56]. It is because, in the yielding of total energy from pairwise potential, an accompanying volume dependent energy [57] has to be introduced in calculation to describe the elastic properties of a metal. An ambiguity about the volume may invalidate the results of a pairwise potential calculation. In other words, the inaccuracy of elastic properties of the solid from the potential may be induced from the uncertain determination of the volume on an atomic scale in terms of defects. For

example, in the process of calculation of fracture, it is often difficult to clearly decide whether to include the volume of the crack and to what extent at internal surfaces. Thus this inaccuracy can be brought into the simulation of the defects, in our case, the crystal-melt interface.

The EAM (short for the embedded atom model) potential, developed by Daw and Baskes [56], takes into consideration the fractures, surfaces, impurities and alloying element. In EAM potential, all atoms are regarded as being embedded in the host lattice consisting of all other atoms. Unlike the volume dependent problem in pair potential, the embedded energy depends on electron density by adding an embedded energy term,

$F\left(\sum_{i \neq j} \rho(r_{ij})\right)$  as in the equation 2.5.

$$E_i(r) = F\left(\sum_{i \neq j} \rho(r_{ij})\right) + \frac{1}{2} \sum_{i \neq j} \phi(r_{ij}) \quad (2.5)$$

In this expression, the potential energy of an atom  $E_i(r)$ , consists of two parts. The second term of the equation, standing for host lattice relaxation  $\phi(r_{ij})$ , can be calculated from pair potentials. Compared with volume on an atomic scale at surface or other defects, the density is always definable. This method circumvents the volume dependent problem because the definable electron density can lead to more accurate elastic properties of the solid. EAM potential is a semi-empirical method. Some functions as embedded energy  $F$  and electron density  $\rho$ , are related to certain properties of the solid. The functions can be determined by empirically fitting them to properties of the bulk metals. In general, the EAM potential incorporates significant many-body interactions and is popular in the

calculation of metallic defects. Thus, we choose to use EAM potential in our simulation of crystal-melt interface of Mg.

Several empirical potentials for Mg had been published [58-63], and recently a more accurate EAM potential was developed by Liu, Adams et al. [16] in 1996. In their approach, they combined both the advantages of ab initio (force-matching method [64]) and empirical methods, by fitting it to a great number of ab initio forces and experimental data. On one hand, the ab initio forces database is comprised of many different structures at certain temperatures, such as bulk, cluster, liquid and some defects, and extensive samples of these structures were obtained to ensure accurate modeling and high transferability [64]. On the other hand, compared with previous EAM potentials for Mg fitted to only a few bulk properties, their potential not only used the lattice constant, cohesive energy and elastic constants, but also a wider range of experimental data, such as vacancy formation energy, stacking fault energy and surface energy, etc. [16]. The extensive forces information and rich experimental data ensured the optimized EAM potential had improved stacking fault energy, good thermal properties and good forces matching. It was then used in fitting to the Mg-Al alloy interatomic potential [16].

In our investigation of pure Mg melted to form solid-liquid interface, both the melting temperature of pure Mg and phase stability around melting point are of great importance for accurate results from our simulation. However, in Liu's EAM potential, the melting temperature of pure Mg is as low as 745K, almost 180K lower than the known melting point of 923K [65]. Moreover, according to Liu's potential, the BCC melting temperature of Mg is 766K [17], about 20K higher than its HCP melting point.

This indicates that a stable BCC solid structure will form from an HCP structure before it will be completely melted into liquid. Besides, a roughly BCC to HCP transition temperature,  $T^{hcp-bcc}$ , of 645K under zero pressure [17] was obtained in Liu's potential and this predicts roughly a 140K temperature interval in which the BCC structure remains much more stable than the HCP before melted. Although there are BCC-HCP transition temperatures at high pressures [66], this BCC stability obviously contradicts the experimental phase diagram of Mg at ambient pressure.

These two major concerns, the much lower melting temperature and contradicted BCC stability just before melting, triggered a newly developed EAM potential for Mg by Sun et al. [17] in 2006, while calculating the crystal-melt interfacial free energy of Mg. In order to apply an empirical potential of Mg to MD simulations of crystal-melt interface with a more accurate melting temperature and the correct crystal structure under the crystal-melt coexisting condition, Sun and his coworkers developed a new potential of Mg. As similar with Liu's procedure [16], Sun also combined the advantages of both the first principle forces calculation [64] and empirical experimental data. In addition to those fitting processes, a re-optimization procedure of Sturgeon and Laird [67] was employed to fit the Mg melting point to the experimental value, to obtain correct liquid density at the melting temperature and to ensure a lower value for the BCC melting temperature than that of the HCP. From all aspects, the results of the newly developed potential generally show a good agreement with experimental data of structural and thermal properties of Mg. Although the Sun's new potential provides slightly poorer values of crystal constants compared with Liu's potential, the melting temperature, indicated to be

914K [17], is significantly improved and very reasonable according to known experimental data. Moreover, the new potential also provides a correct stability of the HCP structure relative to BCC up to the melting temperature. Finally, from previous discussion about all the potential energies, the Sun's EAM potential is chosen to be employed in our simulation of structural and thermal properties of crystal-melt interface of Mg.

### 2.1.2 Ensembles

Ensemble is a term from statistical mechanics, a statistical representative set of configurations. An ensemble can be defined as a whole collection of a very large number of systems in different possible microscopic states that the real system might be in, but all with common observed macroscopic attributes. For example, each system of the canonical ensemble must have the same temperature  $T$ , volume  $V$  and number of particles  $N$  as the real system it represents.

In molecular dynamics simulations, we study a group of particles that can simply be represented by an ensemble of classical mechanical systems. In statistical mechanics, in an ensemble of classical mechanical systems, a collection of elements can be regarded as a group of representative points  $X$ , in the phase space  $\mathcal{A}$ . The statistical properties of a kind of ensemble can be characterized by a correspondent state probability function  $p_i$ . An ensemble average value of a macroscopic property  $\langle f \rangle$ , can be defined over the phase

space  $\Lambda$  in equation 2.6. On the other hand, the time average value of  $f_{t=\infty}$  of a representative point  $X$  in the phase space can be defined over a time interval  $t=\infty$  in equation 2.7.

$$\langle f \rangle = \int_{\Lambda} f_i dp_i \quad (2.6)$$

and

$$f_{t=\infty} = \lim_{t \rightarrow \infty} \frac{1}{t} \int_0^t f(X) dt \quad (2.7)$$

As long as the time interval is infinitively large enough, the ensemble average  $\langle f \rangle$  will equals to the time average  $f_{t=\infty}$ . This equivalence is called ergodic hypothesis and is commonly used in processes involved in ensemble calculations [68].

Ensembles, differentiated by each status probability function  $p_i$ , can be denoted and represented by different macroscopic properties, such as number of particle  $N$ , temperature  $T$ , pressure  $P$ , volume  $V$ , total energy  $E$  and chemical potential  $\mu$ , etc. Each molecular dynamics simulation is performed under designated constraints of environment. In other words, the ensembles are specified in order to get the desired results. Thermodynamic ensembles can be defined according to different physical requirements. Some common ensembles that will mostly be used in our simulation are briefly introduced next.

Canonical ensemble or  $NVT$  ensemble is an ensemble with fixed volume  $V$ , number of particles  $N$  and temperature  $T$ , equilibrated with a heat bath with the same temperature. This ensemble will be used in situations where closed systems require no

fluctuation of volume and also remain in a constant temperature. It can also prevent explosion of the particles even with a large pressure. [69]

Isothermal-isobaric ensemble or  $NPT$  ensemble is closed systems with constant pressure  $P$  and temperature  $T$ . It is important for systems in a constant pressure situation. In our simulation, this ensemble is of great importance in equilibrating crystal-melt system at a constant low pressure and a constant melting point. [69]

Microcanonical ensemble or  $NVE$  ensemble is closed systems with fixed volume  $V$  and total energy  $E$ . This ensemble is also significant because in MD dynamics simulations, in our experience the stabilized volume and energy can greatly help to maintain a much stable equilibrium state in order to obtain more accurate data of thermodynamic properties. [69]

Isoenthalpic-isobaric ensemble or  $NPH$  ensemble is also closed systems with fixed pressure  $P$  and enthalpy  $H$ . In our simulation, this ensemble can help to obtain the melting temperature at crystal-melt systems at a constant pressure. [69]

Grand canonical ensemble or  $VT\mu$  ensemble represents open systems, where the number of particles can change, with constant volume  $V$ , temperature  $T$  and chemical potential  $\mu$ . This ensemble is not employed in our simulation because the whole process of our simulation is in a closed system. [69]

### **2.1.3 Simulation Box in the Simulation Process**

As in previous studies, the two low index planes (0001) and  $(11\bar{2}0)$  are most investigated in previous MD simulation [17-19] (together with  $(1\bar{1}00)$ ), where (0001) is the most compact basal plane and  $(11\bar{2}0)$  lies parallel to the  $c$  axis. A third low index orientation  $(1\bar{1}01)$ , instead of the  $(1\bar{1}00)$  of prior investigations, is chosen in this work in order to examine the behavior of a crystal plane inclined to both the  $a$  and  $c$  axes. The MD simulation cells are generated with periodic boundary conditions along all three spatial directions and these block-shaped boxes are constructed with lengths around 50-70 Å along both the  $x$  and  $y$  axes and 210-250 Å along  $z$  axis, which is normal to the solid-liquid boundary. We choose system sizes of 32000, 40000 and 33280 atoms for (0001),  $(1\bar{1}01)$  and  $(11\bar{2}0)$  orientations respectively.

## 2.2 Structural Characterization of Solid-Liquid Interface

In the analysis of crystal-melt interfaces at the atomic level, there are several characterization methods generally in use and the following are applied specifically in this work to offer a detailed picture of the solid-liquid interfacial structure of Mg crystal and its melt. In our simulation, the direction denoted by  $z$  is normal to the crystal-melt interface and  $x$ ,  $y$  directions are parallel to the interface respectively. In particular we monitored the variation of several important parameters as a function of distance across the interface, i.e. the  $z$  direction, by averaging over the  $x$ - $y$  plane. The atomic structure of the crystal-melt interface can be characterized by a number of profiles defined as follows.

### 2.2.1 Fine-grained Density

The fine-grained density profile is defined [42] as:

$$\rho(z) = \frac{\langle N_z \rangle}{L_x L_y \Delta z} \quad (2.8)$$

where  $N_z$  denotes the number of atoms in a given  $xy$  plane and the angle brackets refer to an average over time of a large number of configurations in a long time run. The system is divided into bins with small volumes along interface normal, and  $\Delta z$  is the bin thickness along  $z$  direction.  $L_x$  and  $L_y$  are length of the system along the  $x$  and  $y$  directions respectively. The bin thickness was set to be 1/40 of the interplanar crystal spacing for each orientation, roughly about 2.65, 2.48 and 1.63 Å for (0001), (1 $\bar{1}$ 01) and (11 $\bar{2}$ 0) respectively.

Due to thermal fluctuations, the mean interface position will vary over the course of an MD run and care must be taken in averaging snapshots over time. In this work we used the procedure outlined by Yang et al. [70]. Due to the instantaneous movement of the interface, the position of interface of each configuration has to be lined up to secure reliable values near interface. An order parameter is defined for this purpose. Commonly, the crystal possesses an ordered state while liquid does the opposite. The difference in order is a usual way to separate solid and liquid phases and to gather information of interface between them. There are three kinds of order parameters generally used in previous studies in this field: orientational order from Davidchack and Laird [42], local order parameter from Hoyt et al. [47], and local order parameter involving wave vectors

from Morris et al. [71]. Other than these, there are more schemes of order parameter relatively less used [72-74]. In this study, local order parameter from Hoyt et al. is chosen, because compared with others this one is more accurate and with more distinct change from solid to liquid especially in our system. It is initially defined [47] in calculation of  $\gamma$  in the FCC system and here applied to our HCP system with slight modification. For each atom in the system, it has an order parameter

$$\phi = \frac{1}{N} \sum_i^N |\vec{r}_i - \vec{r}_i^{hcp}|^2 \quad (2.9)$$

where  $N$  is the number of calculated neighbors of the center atom and  $\vec{r}_i$  is the vector from center atom to the neighbor  $i$  while  $\vec{r}_i^{hcp}$  is vector pointing to the ideal crystal lattice site of neighbor  $i$ . In an ideal case of hexagonal close-packed (HCP) structure with  $c/a$  ratio of 1.633, there are 12 nearest neighbors for a given atom with a zero value of  $\phi$ . However, in a real case of crystal like ours with  $c/a$  ratio of 1.631, it is easy to estimate that due to deviation of  $c/a$  ratio from 1.633 and thermal atomic oscillations near its lattice site, the number  $N$  within a pre-defined region might vary near 12, and the value of  $\phi$  will be near but slight above zero for solid. The interface position is defined by the position with a  $\phi$  value both half way to that of bulk solid and liquid. In our simulation,  $\phi_{solid}$  and  $\phi_{liquid}$  are about 0.2 and 1.4 and thus  $\phi_{interface}$  is around 0.8. It is used to line up the fine-grained and stress profile, that will be introduced next, and to determine roughly the interface position for the excess energy calculation. Briefly, the solid-liquid interface position for each snapshot was determined from an order parameter profile as described by Hoyt et al. [47]. The origin along  $z$  was further refined by locating the fine grain density peak closest

to the interface position predicted by the order parameter analysis and shifting the peaks to the  $z=0$  point.

### 2.2.2 Coarse-grained Density

The coarse-grained density profile resolves peaks due to individual crystalline planes. To obtain a description of quantities such as the interface width, a coarse-grained density, described by Davidchack and Laird [42], is often used. The coarse scale density profile is constructed through a numerical recipe called the finite impulse response (FIR) filter [75]:

$$\bar{f}_i = \sum_{k=-n}^n w_k \cdot f_{i+k} \quad (2.10)$$

where  $\bar{f}_i$  is the filtered value of the coarse scale type at position  $i$ , and  $f_{i+k}$  is the fine scale density value of neighbor  $k$  within a selected range ( $\pm n$ ). The parameter  $w_k$  is the filter coefficient generally configured to be a Gaussian form:

$$w_k = A e^{-(k/\varepsilon)^2} \quad k=-n, \dots, n, \quad (2.11)$$

where  $A$  is the normalization coefficient defined as:

$$A = \frac{1}{\sum_{k=-n}^n e^{-(k/\varepsilon)^2}}. \quad (2.12)$$

The  $n$  and  $\varepsilon$  value can be evaluated from a minimizing process of the quantity:

$$S = \sum_i (\delta^2 \bar{f}_i)^2 \quad (2.13)$$

where 
$$\delta^2 \bar{f}_i = \bar{f}_{i+1} + \bar{f}_{i-1} - 2\bar{f}_i. \quad (2.14)$$

We can choose  $n$  and corresponding  $\varepsilon$  via a plot of  $S$  versus  $\varepsilon$  plot for different  $n$ . In our simulation, when  $n=80$ , fine oscillations can be generally smoothed. Starting from  $n=80$ , we extend the analysis to  $n=100$  and  $n=120$ , as shown in Fig. 2.3 for the (0001) orientation. It is obvious that the minimum value of  $S$  decreases when  $n$  increases and it reaches its minimum at  $n=120$  and  $\varepsilon=42.5$ . We find both the  $(1\bar{1}01)$  and the  $(11\bar{2}0)$  orientations have the same trend as (0001), with an identical  $\varepsilon$  value at the minimum in  $S$ . Thus this set of parameters is employed to obtain the coarse-grained density profiles for three orientations.

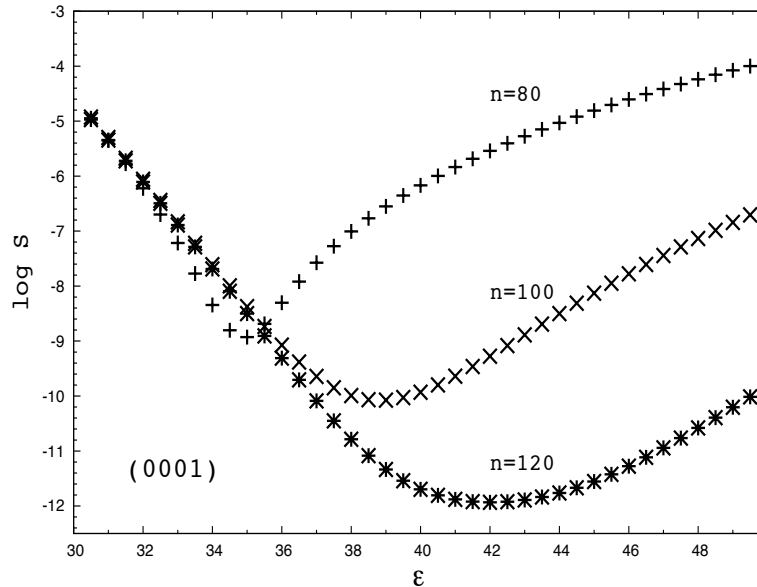


Fig. 2.3: Logarithm  $S$  versus  $\varepsilon$  for  $n=80, 100, 120$  for (0001) orientation illustrating the procedure for determining optimal values in the FIR filter function.

With coarse scale density profile, the 10-90 width of the interface,  $w_{10-90}$ , an important index characterizing the thickness of solid-liquid interfacial structure, can be determined. The 10-90 width is constructed by determining the  $z$  position where a given quantity (e.g. coarse-grained density) is 10% of the distance between the solid and liquid values, and second  $z$  position where the quantity is 90% of the distance as the expression in equation 2.15, where the  $v_{solid}$  and  $v_{liquid}$  represent the value of solid and liquid in a certain profile respectively. The difference between the two  $z$  points is the  $w_{10-90}$ .

$$10\% \cdot |v_{solid} - v_{liquid}| \rightarrow 90\% \cdot |v_{solid} - v_{liquid}| \quad (2.15)$$

### 2.2.3 Layer Separation

Layer separation [42] is the study of the spacing variation between adjacent crystalline layers in the direction normal to the interface, across interface region. The spacing variation is defined simply as:

$$\Delta Z_i = \langle Z_{i+1}^{peak} \rangle - \langle Z_i^{peak} \rangle \quad (2.16)$$

where the angle bracket denotes the time average position of each peak in the fine scale density profile. Previous work on BCC and FCC structures have shown interesting features in the layer separation function for different interface orientations and thus, in Chapter 4 of this work, results of HCP Mg will presented and compared with cubic systems.

### 2.2.4 Interface Stress Profile

The interface stress,  $\tau$ , is the variation in the interfacial free energy with respect to interfacial strain [76] and can be expressed as [49]:

$$\tau = \gamma + A \frac{\partial \gamma}{\partial A} \quad (2.17)$$

where  $\gamma$  is the interfacial free energy and  $A$  is the interface area. From this equation, it is possible that  $\tau$  can be a positive number, larger or smaller than  $\gamma$ , or even a negative due to the second term, while  $\gamma$  can never be [45]. Recent atomistic simulations show that  $\tau$  of solid-liquid interfaces can be positive (in the expansion state) or negative (in compression) with different material [77].  $\tau$  with a unit of force per unit length, is described by Gibbs [45] as the work spent in stretching the surface and is also described by Cahn [48] to apply to a thin wafer to make all stress vanish. In simulations [77], because the structural incompatibility between solid and liquid after melting with the fixed size of the interface, the stress is arisen that it tends to expand (or shrink) the interfacial area and this stress can play a vital role in a number of phenomena such as nucleation processes [77].

The interface stress also can be found by integrating from negative infinity to positive infinity of the function:

$$S(z) = P_{zz}(z) - \frac{P_{xx}(z) + P_{yy}(z)}{2} \quad (2.18)$$

$$\tau = \int_{-\infty}^{+\infty} S(z) dz \quad (2.19)$$

Where  $P_{zz}$  is the virial pressure normal to the interface and  $P_{xx}$  and  $P_{yy}$  are the transverse pressures. It can be regarded as integrand and integrated along interface normal to obtain the excess interfacial stress  $\tau$ , which is also an important input parameter in our estimation of temperature dependence of  $\gamma$  under non-equilibrium condition as introduced in thermodynamics section of this chapter. Different from the previous study [42] which using temperature profile and velocity to indirectly get stress component with a lot of computation, we use commands in LAMMPS [78] code with few effort of computation to directly compute and print out the stress tensor components as stress-times-volume form on a per atom base, and then convert them to the averaged stress components varying along interface normal. The bin process is similar to that of the density profile. According to interface position defined by order parameter  $\phi$ , we have averaged the three pressure components for a total of 30 bins spanning the interface position and the averaging window for each bin was taken as the interplanar spacing for each orientation, with  $\Delta z$  for each bin of about 2.65, 2.48, 3.25 Å in (0001), (1 $\bar{1}$ 01) and (11 $\bar{2}$ 0) respectively.

### 2.3 Interfacial Free Energy $\gamma$

The interfacial free energy  $\gamma$  is one of the most critical factors in the study of the solid-liquid interface. In this part, we first begin with the previous research on interfacial free energy  $\gamma$ , by introducing its experimental measurements, its importance of anisotropy, the obtaining of its anisotropy by experimental methods, and its temperature

dependence. Second, we introduce the thermodynamic integration technique, so called Gibbs-Cahn integration, as a method to be used in our estimation of temperature dependence of  $\gamma$  at non-equilibrium temperatures.

### 2.3.1 Previous Research

Interfacial free energy [45] is defined as the reversible work necessary to create a unit area of interface. Due to the presence of the interface, the excess free energy [48] is the difference between the Gibbs free energy of a system containing a unit area of interface and that of the bulk phases of which the system consists. If the system contains an interface with an area of  $A$ , the excess free energy is given by

$$\gamma A = G - G_{bulk} = (E - TS + PV) - \sum_m \mu_m N_m \quad (2.20)$$

where  $E$ ,  $T$ ,  $S$ ,  $P$ ,  $V$  is the internal energy, temperature, entropy, pressure and volume of the system respectively.  $\mu_m$  is the chemical potential of a species  $m$  and  $N_m$  is the number of this particular species.

#### 2.3.1.1 Experimental Measurement

In the middle of 20th century, the solid-liquid interfacial free energy  $\gamma$  was extracted experimentally [10] by Turnbull from the homogeneous nucleation rates at temperatures close to their maximum undercooling when he studied the formation of

crystal nuclei in liquid metals. That is one of the oldest and most utilized techniques for the determination of  $\gamma$ . In that work, Turnbull compiled  $\gamma$  from various nucleation experiments and proposed an important empirical relation between  $\gamma$  and the latent heat of fusion as shown in Equation 2.21: the interfacial free energy  $\gamma$  properly scaled by the number density of solid  $\rho_s$  is proportional to the molar latent heat of fusion,  $\Delta H_{fus}$ ,

$$\gamma \rho_s^{-2/3} N_A = \alpha \Delta H_{fus} \quad (2.21)$$

where  $N_A$  is the Avogadro's number and  $\alpha$  is the Turnbull coefficient. The left side of the equation 2.21 represents an effective interfacial free energy of an area with a mole of atoms. The Turnbull coefficient  $\alpha$  was found to be approximately 0.45 for metals and 0.32 for many nonmetals and semi-metals and the coefficient for metals has been confirmed by MD simulations in Hoyt et al.'s paper [122]. Thus, theoretical models of crystal-melt interface can use this empirical Turnbull relation as an important check and also this relation can be used as an approximation of  $\gamma$  where the direct measurement of  $\gamma$  is unavailable.

Other than this Turnbull extraction measurement from the nucleation frequencies and maximum undercooling, there are many other experimental methods, from which the interfacial free energy  $\gamma$  can be determined, such as the measurements of dihedral angles by Glicksman and Vold [5, 79], the measurements of contact angles and the depression of melting points in small particles, described in a review by Eustathopoulos [80] and last but not least, the grain boundary groove method, an extensively used approach discussed by Napolitano et al. [81].

### 2.3.1.2 Anisotropy and its Experimental Measurement

Although previous various experiments can be employed to extract an estimation of interfacial free energy  $\gamma$ , the results are averaged over all crystal orientations [81] and thus are not very accurate in terms of the differences between planes with different crystal orientations.

Although the anisotropy of interfacial free energy  $\gamma$  for solid-liquid interfaces is very weak in metals, it has been proved through theory [82-86], experiment [87] and computational simulations [88-90] that anisotropy of interfacial free energy  $\gamma$  is critical to the selection of the operating states of the dendritic tip in the solidification process. The operating states of dendrite tips [89] include velocity  $v'$  and tip radius  $r'$  and in the simulation work of Wang and Sekerka [89], the corresponding tip radius  $r'$  increased with supercooling for anisotropy of interfacial free energy  $\gamma$  and tip growth velocity  $v'$  was found to increase with the increased anisotropies of  $\gamma$ . Thus, a successful description of the solidification process requires an accurate calculation of the anisotropy of the interfacial free energy.

There have been a few experiments [81, 91-94] to determine the anisotropy of the interfacial free energy  $\gamma$ . Since some of them [91-93] were performed in transparent organic materials, quite different from our interests of metals, we particularly focus on the

studies of the alloy systems [81, 94] by Napolitano et al. In their studies of two alloy systems, Al-Cu and Al-Si, an experimental method for the measurement of the anisotropy of the crystal-melt interfacial free energy  $\gamma$  was developed. They presented a theory [81] for the equilibrium shape of a coupled grain boundary groove at the crystal-melt interface. Through the examination of the equilibrium shape of liquid inclusions, the anisotropy of the interfacial free energy was computed. In General, this experimental practice [81] by Napolitano significantly reduced the uncertainty of anisotropy of crystal orientations in terms of previous experimental calculations of interfacial free energy  $\gamma$  and provided an experimental approach in determination of the important weak anisotropy of  $\gamma$  in metals.

### 2.3.1.3 Temperature Dependence of $\gamma$

Under equilibrium conditions, the temperature dependence of the interfacial free energy  $\gamma$  has been known from the work of Gibbs [45, 48]:

$$\frac{d\gamma}{dT} = -S_{ex} \quad (2.22)$$

where  $T$  is the temperature, and  $S_{ex}$  is the excess entropy, the entropy difference between the system containing the solid-liquid interface and the bulk with respect to a Gibbs dividing surface that corresponds to zero excess volume  $V_{ex}$  [48].

The temperature dependence of  $\gamma$  for metals was first discussed by Turnbull [85] who found an increase in  $\gamma$  with temperature in the study of solidification of mercury. In that paper, he pointed out  $\gamma$  must increase with temperature if the atomic jump frequency

was to have a physically reasonable value. From equation 2.22, the increase relation must result in a negative excess entropy value  $S_{ex}$  and this, in the review from Spaepen [96], is explained with a loss of entropy of the interface with respect to the liquid side of the system as illustrated in Fig. 2.4. In this figure, it is very obvious that the loss of entropy or the negative value of excess entropy is resulted from the quite slow rise of the system entropy across the interface to the liquid.

In Fig. 2.4, the superscripts refer to the values in the bulk phases, with  $\alpha$  denoting the bulk solid and  $\beta$  the bulk liquid. The  $-S_{ex}$  is equal to the temperature dependence of  $\gamma$  and the dividing surface must be chosen to give zero excess volume  $V_{ex}$ .

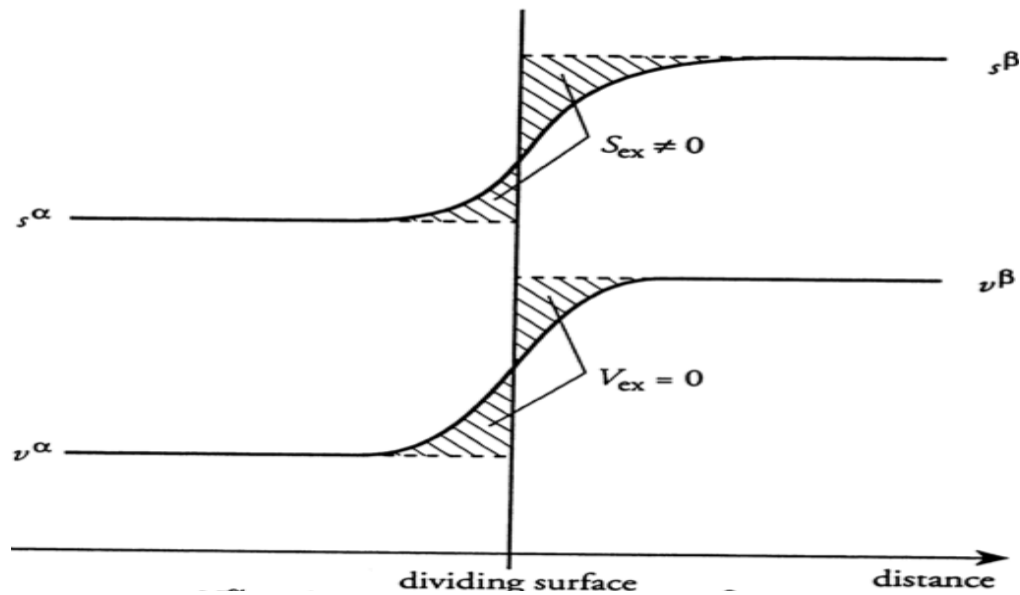


Fig. 2.4 Diagram of the molar volume  $v$  and molar entropy  $s$  across the interface [96]

This positive temperature dependence of  $\gamma$  is consistent with the negative values of the excess entropy  $S_{ex}$  from several phenomenological and structural models of the

solid-liquid interface [96-107], density functional theory [108, 109] and recent simulation results [46, 110] for pure systems. In Spaepen's reanalysis [96] of the experimental data for the temperature dependence of  $\gamma$  in mercury [95] and gallium [111], he attributed the positive temperature dependencies as being associated with a negative excess entropic contribution to  $\gamma$ .

### 2.3.2 Thermodynamic Integration Technique

As mentioned in chapter one, the excess interfacial free energy of the solid-liquid interface in EAM Mg has been determined using the capillary fluctuation method. Our primary interest in the current investigation is the temperature dependence of  $\gamma$ . In our work, we study on a block system with periodic boundary condition completely containing a planar interface, to which the  $z$  direction is normal and  $x, y$  directions are parallel. The solid is in contact with liquid phase at a pressure  $P$  along  $z$  direction. The differential form of excess free energy  $\gamma A$  thus can be deduced [49] to

$$d(\gamma A) = -SdT + VdP - \sum_m N_m d\mu_m + \sum_{i,j=1,2} (\sigma_{ij} + \delta_{ij}P) V d\varepsilon_{ij} \quad (2.23)$$

where  $\sigma_{ij}$ ,  $\varepsilon_{ij}$  and  $\delta_{ij}$  are the average stress, strain tensors and Kronecker symbol, respectively of components  $i$  and  $j$ . Components  $i$  and  $j$ , identical to  $x$  and  $y$ , represent the directions perpendicular to interface normal,  $z$  direction. In the solid-liquid system, analogous equations can be expressed in the form of Gibbs-Duhem equations for bulk solid and liquid:

$$0 = -S^s dT + V^s dP - \sum_m N_m^s d\mu_m + \sum_{i,j=1,2} (\sigma_{ij}^s + \delta_{ij}P) V^s d\varepsilon_{ij} \quad (2.24)$$

$$0 = -S^l dT + V^l dP - \sum_m N_m^l d\mu_m \quad (2.25)$$

where the lower case  $s$  and  $l$  denote bulk solid, liquid quantities respectively. Particularly for solid under hydrostatic conditions, equation 2.24 can be simplified to equation 2.26 similar to equation 2.25 for liquid.

$$0 = -S^s dT + V^s dP - \sum_m N_m^s d\mu_m \quad (2.26)$$

Cramer's rule was applied in Cahn's paper [48], on equations above to derive an expression for  $d(\gamma A)$  and therefore it took the form [41, 49] of

$$d(\gamma A) = -[S/NV]dT + [V/NV]dP - [N/NV]d\mu + \sum_{i,j=1,2} [(\sigma_{ij} + \delta_{ij}P)V/NV]d\varepsilon_{ij} \quad (2.27)$$

where the denotation of the value in bracket is, take entropy  $S$  for example:

$$[S/NV] \equiv \frac{\begin{vmatrix} S & N & V \\ S^s & N^s & V^s \\ S^l & N^l & V^l \end{vmatrix}}{\begin{vmatrix} N^s & V^s \\ N^l & V^l \end{vmatrix}} \quad (2.28)$$

Note that in derivation of equation 2.28 by Cramer's rule,  $d\mu$  and  $dP$  are chosen to be two unknowns and thus can be eliminated in expression for the third unknown  $d(\gamma A)$  by the value of each determinant which equals zero according to definition. Moreover, in our work, we study on a system where both bulk solid and liquid starting to be fixed to the zero pressure in all three directions, that is, under hydrostatic conditions.

$$\sum_{i,j=1,2} [(\sigma_{ij} + \delta_{ij}P)V/NV] = \sum_{i,j=1,2} \frac{\begin{vmatrix} (\sigma_{ij} + \delta_{ij}P)V & N & V \\ 0 & N^s & V^s \\ 0 & N^l & V^l \end{vmatrix}}{\begin{vmatrix} N^s & V^s \\ N^l & V^l \end{vmatrix}} = \sum_{i,j=1,2} (\sigma_{ij} + \delta_{ij}P)V \quad (2.29)$$

Thus, equation 2.29 finally takes the form

$$d(\gamma A) = -[S/NV]dT + \sum_{i,j=1,2} (\sigma_{ij} + \delta_{ij}P)Vd\varepsilon_{ij} \quad (2.30)$$

Furthermore, first, because the interfaces studied here are in possession of high symmetry, where  $\sigma_{12}=0=\sigma_{21}$ . Second, along the temperature variation  $dT$  on a non-equilibrium condition, if we assume the system experiences expansion while keeping same shape, the strain variation has the relation:  $d\varepsilon_{11}=d\varepsilon_{22}$ . Since on the area  $A$  of interface,  $d\varepsilon_{11}+d\varepsilon_{22}=dA/A$ , we can get  $d\varepsilon_{11}=d\varepsilon_{22}=dA/2A$ . Third, according to Cahn [48], the  $[S/NV]$  is the excess entropy value between system and bulk phases for an interface area of  $A$ , and it can be represented by excess internal energy  $e$ , between system completely containing a unit area of interface and bulk phases, by a treatment from Frolvo and Mishin [49].

With respect to above reasons, the expression can be written [41] as

$$\frac{1}{A} d(\gamma A/T) = -\frac{e}{T^2} dT + \frac{\tau}{T} \frac{dA}{A} \quad (2.31)$$

where  $A$  is the area of interface and  $\tau$  can be obtained from equation 2.19. In light of this treatment [41], according to the assumption that system expands in same shape with  $dT$ , the density of solid phase  $\rho_s$  and interfacial area  $A$  has the relation of:

$$A = K \cdot (\rho_s)^{-\frac{2}{3}} \quad (2.32)$$

where  $K$  is a constant coefficient. The equation 2.32 is substituted to equation 2.31 and divided by  $dT$ , which in our case is a temperature variation under non-equilibrium/coexistence condition at zero pressure. Thus, the equation 2.31 can be expressed in terms of the number density of the solid.

$$\frac{d[(\rho_s^{-\frac{2}{3}} \gamma)/T]}{dT} = -\rho_s^{-\frac{2}{3}} \left( \frac{e}{T^2} + \frac{2\tau}{3\rho_s T} \cdot \frac{d\rho_s}{dT} \right) \quad (2.33)$$

The variation of  $\rho_s$  with temperature can be easily computed in MD simulations of the crystal phase. In our estimation of temperature dependence of  $\gamma$ , it's very difficult to get  $e$  and  $\tau$  at a non-equilibrium temperature by simulation, since these quantities are often obtained from statistics of long equilibrium runs. Thus in our case, we use  $e$  and  $\tau$  at the melting temperature and zero pressure approximation to estimate the values at non-equilibrium temperatures, which means  $e$  and  $\tau$  values below the melting temperature. The relation of  $\rho_s$  with  $T$  within a range of temperatures is available from MD simulations.  $\tau$  can be obtained by integrating stress defined in previous stress profile along  $z$  direction, which is also available from interfacial structure information by MD simulations of this work. Defined via a concept of Gibbs dividing surface [45], the quantity  $e$  in the above equations is the excess energy of the crystal-melt interface and using the definition of the Gibbs dividing surface,  $e$  can be written as:

$$e = \frac{1}{2A} [E - A(\rho_s^E L_s + \rho_l^E L_l)] \quad (2.34)$$

where  $E$  is the total energy of the system completely containing the interface.  $\rho_s^E$  and  $\rho_l^E$  are energy density of solid bulk and liquid and can also be obtained from interfacial structure information of the previous potential energy profile and the factor of 2 arises due to the fact that two interfaces are present in the periodic MD cells. The  $L_s$  and  $L_l$  are the lengths of the solid and liquid phases, respectively, in the cell and can be determined from the definition of the dividing surface, which assumes excess number of particles over bulk to be zero, which means total number of particles in system are the same with the sum of that of bulk solid and liquid and leads to the following requirements:

$$N = A(\rho_s L_s + \rho_l L_l) \quad (2.35)$$

$$L = L_s + L_l \quad (2.36)$$

where  $\rho_s$  and  $\rho_l$  is bulk solid and liquid density respectively,  $N$  is the total number of atoms and  $L$  is the total length of the system.

It is clear to see that from our study of solid-liquid interfacial structure and by obtaining the  $e$ ,  $\tau$  at melting temperature and  $\rho_s(T)$  over a range of temperature of interest, the so called Gibbs-Cahn integration, integration of the differential equation, can help to estimate the temperature dependence of  $\gamma$  at non-equilibrium temperatures, given a known value of interfacial free energy at melting temperature as a start point of integration. Thus, in our simulation we will employ this thermodynamic integration technique to estimate the temperature dependence of  $\gamma$  at non-equilibrium temperatures.

## CHAPTER THREE

### SIMULATION PROCESS

---

All molecular dynamics simulations utilize the parallel code LAMMPS [78]. A minimum time interval of 0.001 picosecond, called a timestep, is used throughout the whole simulation processes.

### 3.1 Melting Temperature

Before creating a stable crystal-melt structure, the most important step is the determination of the equilibrium melting point for the EAM potential using the coexistence technique by Morris et al. [112, 113]. Although a value of  $T_M=914\text{K}$  has been determined in previous work [17], the process to find the  $T_M$  is still repeated here because it is known that the melting point can vary slightly with system size [114]. After constructing a solid-liquid two phase system at  $T=914$ , we perform a simulation using an isenthalpic ( $NP_zH$ ) ensemble with zero pressure, applied along the  $z$ -axis. This ensemble helps to adjust the temperature to the stable point that can generally maintain the structure component by fixing the total enthalpy of the system at zero pressure. After this step, the system spontaneously moves toward the equilibrium melting point and a value of

$T_M=911\text{K}$  is found. The Mg crystal lattice constants  $a$  and  $c$  values were obtained to be  $3.2522(4)\text{ \AA}$  and  $5.3037(5)\text{ \AA}$  respectively at the melting temperature.

### 3.2 Equilibration of Crystal-Melt Model

Equilibration of all three systems, (0001), (1 $\bar{1}$ 01) and (11 $\bar{2}$ 0) at the melting point was achieved using the procedure outlined in previous publications [112, 113]. Briefly the middle portion along the  $z$  axis was first melted in  $NVT$  ensemble with a temperature much higher than  $T_M$  and then the system subsequently equilibrated for roughly 5 nanosecond in an  $NP_zT$  ensemble at melting temperature  $T_M$ , where the dimensions along  $x$  and  $y$  remained fixed and  $P_z=0$ . During the first  $NVT$  step, the melting of liquid at a higher temperature and fixing of the volume could cause a fairly high pressure in the system. To achieve equilibrium, the  $NP_zT$  ensemble at melting point then could appropriately release the remaining pressure in the liquid at melting point and give a general zero pressure along interface normal,  $z$  axis.

### 3.3 Obtain Data

After equilibration, in order to ensure the data obtained in a very stable condition, we choose a configuration, whose length of box along the  $z$ -axis ( $L_z$ ) and potential energy ( $E$ ) are very close to the statistical averages obtained during equilibration. Starting from this specific configuration, a microcanonical ( $NVE$ ) ensemble is employed for an

additional equilibration of 0.8 nanosecond for each of the three orientations. During this final production run, snapshots of atom positions are obtained every 1000 time steps (1picosecond).

## **CHAPTER FOUR**

### **RESULTS, ANALYSIS AND DISCUSSION**

---

As stated in previous chapters, employed newly developed EAM potential of Mg, the molecular dynamics simulations of three different interfaces were set the simulation procedures and to be run by LAMMPS code. In addition, the simulation data at the equilibrium condition was obtained and analyzed through the characterization methods introduced in Chapter two both in structural and thermodynamic aspects. The analyzed results and discussions are detailed in this chapter.

#### **4. 1 Structure**

In all three interfaces, interfacial widths, layer separations and stress profiles are investigated respectively. Moreover, the anisotropy of these properties have been studied and compared with extensive previous research on other systems. All these results of the structure properties have been discussed.

#### 4.1.1 Interfacial Widths

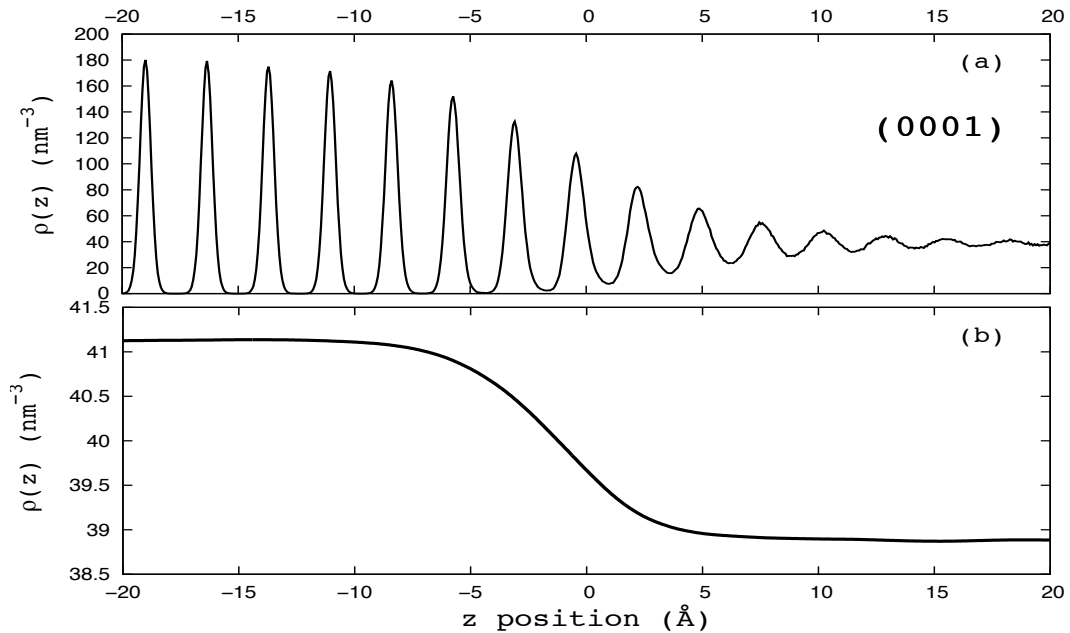


Fig. 4.1: Fine-grained density profile (a) and coarse-grained density profile (b) of the (0001) crystal-melt interface as a function of  $z$  direction, a direction perpendicular to the studied interface.

The fine and coarse-grained density profiles are shown in Figures 4.1-4.3, for (0001),  $(1\bar{1}01)$  and  $(11\bar{2}0)$  interfaces respectively. From fine-grained profiles, the order of peak values of density in different interfaces follows the order of density of the interface in a bulk crystal, which implies that (0001) is the most compact plane while  $(11\bar{2}0)$  the least. The structural width, a term used by Davidchack and Laird [42] indicates the 10-90 width constructed using the 10% to 90 % variation of the peak value of fine-grained

density profile versus the  $z$  position, and as listed in Table 4.1 are the structural widths from fine-grained density profiles.

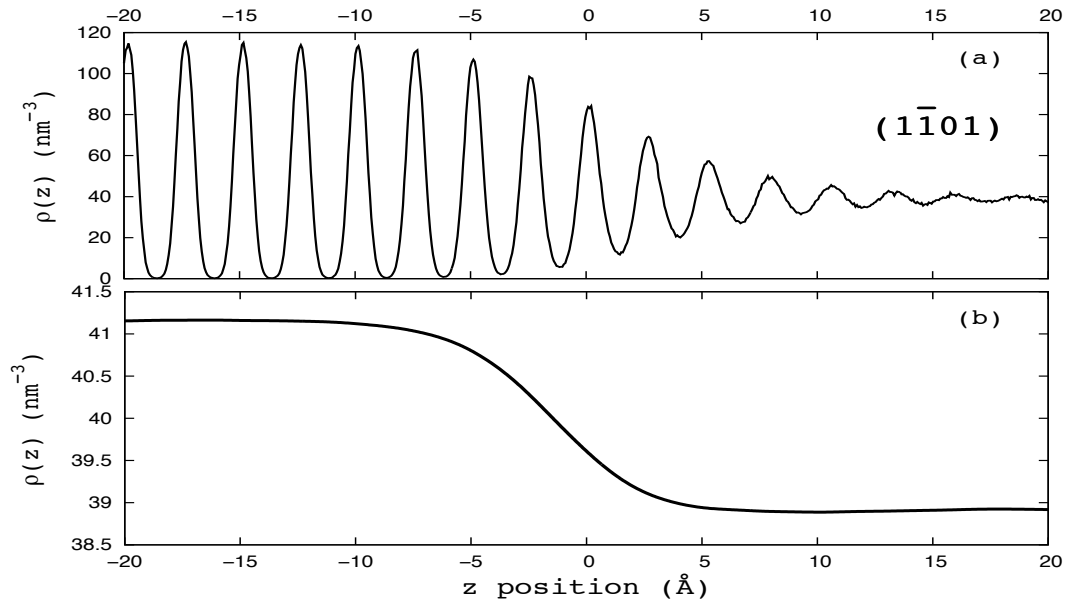


Fig. 4.2: Fine (a) and coarse-grained (b) density profiles of the  $(1\bar{1}01)$  interface along the vertical direction of the interface studied.

The values of parameters  $n=120$  and  $\varepsilon=42.5$  are determined by Fig. 2.3 in order to smooth fine-grained to coarse-grained density. The zero position in  $z$  direction in this paper indicates the position determined by distance both half way to solid and liquid, which is also the position of Gibbs dividing surface. The 10-90 widths from coarse-grained density profiles are listed in Table 4.1 as well and will be discussed.

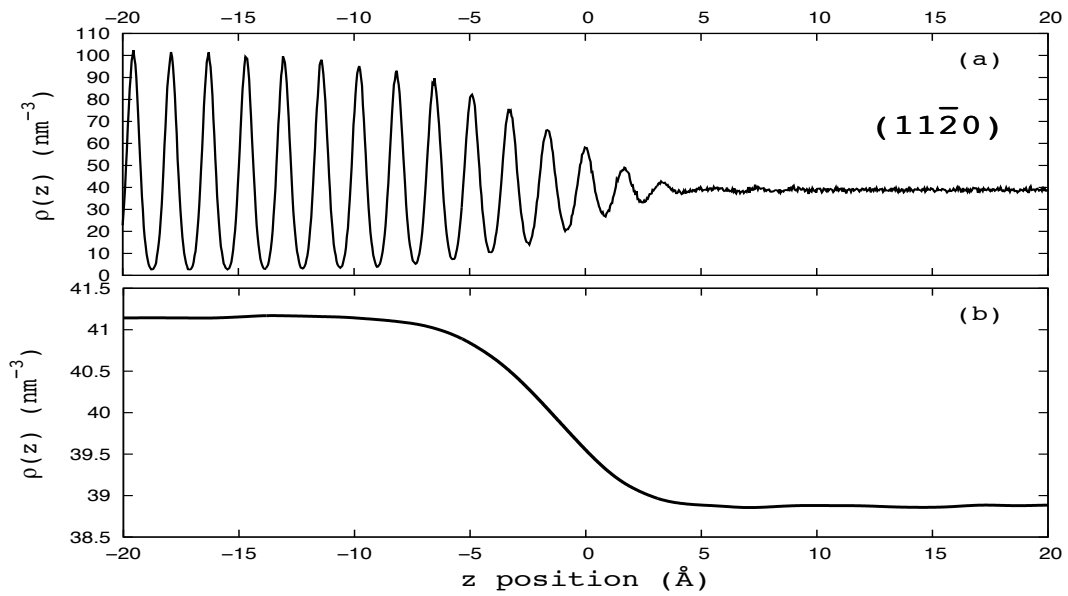


Fig. 4.3: Fine and coarse-grained density profiles of the  $(11\bar{2}0)$  interface along  $z$  direction.

The profiles shown in Fig. 4.4 are potential energy density profiles indicating potential energy density variation from bulk solid to liquid through the interface region for all three interfaces. The same plot was used in Laird and Haymet's work [115] as a tool to study the interface widths. The 10-90 widths of this potential density profiles are also collected in Table 4.1.

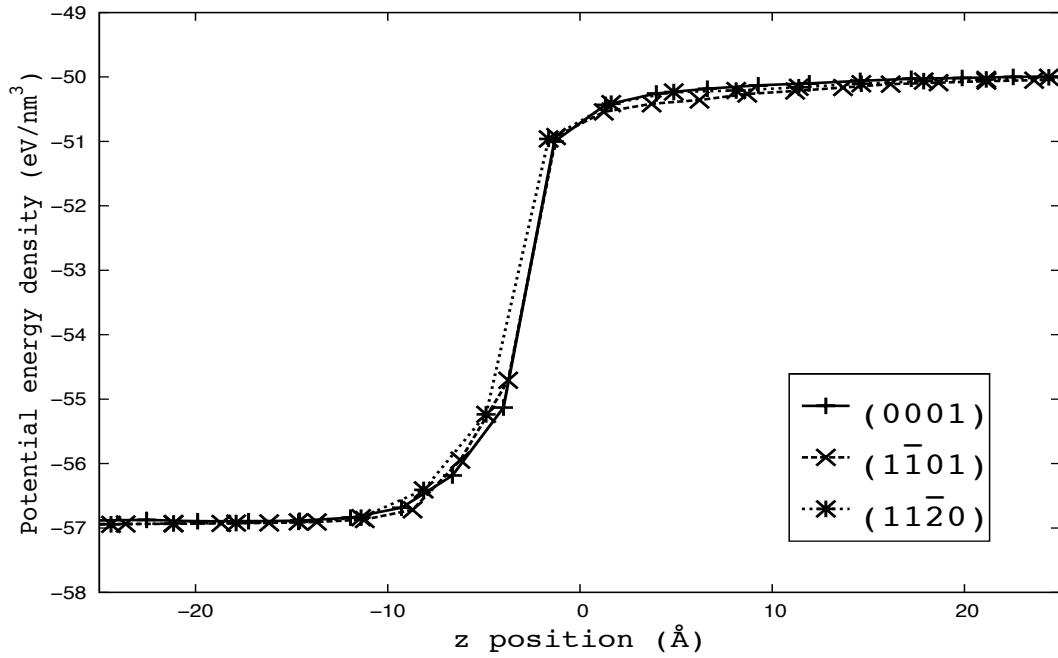


Fig. 4.4: Potential energy density profiles for the three interfaces, defined as the potential energy contained in unit volume as a function of a variety of positions through  $z$  direction.

TABLE 4.1: Interfacial widths from various types of profiles of the three different interface.

Interfacial widths (Å)	Fine-gained profiles	Coarse-gained profiles	Potential energy profiles	Order parameter profiles	Stress profiles
(0001)	16.3	8.5	7.1	9.6	15.9
(1101)	15.7	8.6	7.4	11.0	16.3
(1120)	11.9	7.6	8.1	11.2	15.9

The types of widths include the 10-90 width of fine and coarse-grained profile, the potential energy profile, the order parameter profile and the 10-90 width of stress profile, which particularly defined as the distance between positions where two 10% values of variation in stress profile take possession while crossing the interface from solid to liquid phase.

#### 4.1.1.1 Structural Widths

In terms of various interfacial widths, first it is relatively obvious that according to fine scale density profiles and their corresponding structural widths, the peaks of  $(11\bar{2}0)$  are much earlier diminished on the liquid side (at  $z$  position of about 3 Å) than those of both  $(0001)$  and  $(1\bar{1}01)$  interfaces are (at round 10-15Å). As listed in Table 4.1, the structural widths from fine-grained density profiles are 16.3, 15.7 and 11.9 Å for  $(0001)$ ,  $(1\bar{1}01)$  and  $(11\bar{2}0)$  interfaces respectively. This anisotropy is quite similar to the result from the work of Huitema et al. [116] with a system of FCC Lennard Jones (LJ) particles. In their work, the density oscillation in  $(111)$  and  $(100)$  interfaces, comparable with  $(0001)$  and  $(1\bar{1}01)$  interfaces, last about  $7d_{hkl}$  before die down on liquid side and that of  $(110)$ , which, identical to  $(11\bar{2}0)$ , lasts for only  $5d_{hkl}$ . The reason was explained by Broughton and Gilmer [117], that the fluid structure factor  $S(q)$  was closest to the interlayer spacing of  $(111)$  interface, thus density oscillation with a spacing similar to  $d_{111}$  was created at the lowest energy cost and therefore, could spread longer into liquid. Thus

if this hypothesis also stands for the HCP structure, the interlayer spacing between (0001) and (1 $\bar{1}$ 01) should be identical on the liquid side and spacing of (11 $\bar{2}$ 0) should be less than that of (0001). It is worthwhile to mention that this assumption about interlayer spacing is indeed proved by the results in the content of interlayer separation.

#### 4.1.1.2 Intrinsic Widths

The 10-90 widths are commonly defined by coarse-grained density profiles as intrinsic widths [42] in literature and there exists many investigations that have been done of the 10-90 widths for various systems. From Table 4.1, the anisotropy of these widths is fairly weak compared with that of the previous structure widths (fine-scaled). These 10-90 widths are about 8 Å for all three interfaces, and from the potential parameters [17] in Sun's EAM potential, the cutoff distance  $\sigma$  is around 2.6 Å in general. Thus the intrinsic widths for three interfaces are about  $3\sigma$ . As a comparison, the interface width of the Huitema et al. [116] with the FCC LJ system is around 10 Å or  $3\sigma$  for all (111), (100) and (110) interfaces with a weak anisotropy; The width from Davidchack and Laird [42] of a system consisting of hard sphere particles is around  $3\sigma$  for both (111) and (100); That of binary hard sphere from Davidchack and Laird [118] is  $4\sigma$ ; That from concentration profile of Ramalingam et al. [119] with a EAM potential Cu-Ni alloy system is about 7 Å for both (111) and (100) interfaces; That of Si using Stilling-Weber potential from work of Buta et al. [120] is 6 Å for both (111) and (100) interfaces; That of NaCl like binary hard sphere system of the work of Sibug-Aga and Laird [121] is as well around  $3\sigma$  for

both (111) and (100) interfaces. Although they may belong to different kinds of particle systems and even different crystal structures, the ranges of 10-90 widths from the coarse-grained profile are quite similar. It proves that the results of interfacial widths are reasonable in this simulation. It is also worth to mention that the structure widths in our simulation are twice of the intrinsic widths, and the similar situations are also obtained in hard sphere systems [42, 118] and Si system with a description of Stilling-Weber potential [120].

#### **4.1.1.3 Interfacial Widths from Other Interfacial Profiles**

Besides structure widths and intrinsic widths, 10-90 widths of potential energy density profiles and order parameter profiles, as well as 10-90 widths of stress profiles are also investigated with comparisons. They are also listed in Table 4.1. In works of Huitema et al. [116], Davidchack and Laird [42] and Buta et al. [120], the widths from order parameter profiles are almost the same value as intrinsic widths,  $10 \text{ \AA}$  or  $3\sigma$ . Here in our study of HCP Mg, the widths from order parameter profiles and intrinsic are also similar to each other, around  $7\text{-}11 \text{ \AA}$ , with a weak anisotropy. The widths from potential energy profiles are also studied by Laird and Haymet [115], and they conclude that the interface region defined by the potential energy profile is relatively independent of interfacial orientations. We find that the 10-90 widths from potential energy density profiles indeed also have a weak anisotropy compared with the structural widths and

exhibit almost same values as the intrinsic widths. The 10-90 widths of the stress profiles also show little anisotropy but have similar magnitudes to structural widths derived from fine-grained profiles, around 16 Å for all three interfaces.

#### 4.1.2 Layer Separation

Laird et al. have studied layer separation in the FCC structure [41] in three interfaces (111), (100) and (110). Among the three interfaces, (111) interface in the FCC is the most compact interface, comparable with (0001) in our simulation, (100) is the less compact interface, comparable with  $(1\bar{1}01)$ , and (110) is the least compact of all, comparable with  $(11\bar{2}0)$ . The results from Laird et al. are shown in Fig. 4.5 that the most and least compact interface (111) and (110) have shown almost constant layer spacing across the interface region, while in the (100) interface it is observed a expansion of layer spacing to the value of (111) interface at interfacial region. Thus we are curious that whether this interesting phenomenon will exhibit in the HCP structure in the same way with respect to the comparable orientations. The distance variation of two adjoining peaks near the interface region from the fine-grained density profiles shown in Fig. 4.1-4.3 are summarized and plotted in Fig. 4.6. We find that the (0001) layers have a slight expansion at the interface, but the change is much smaller than the obvious rise in the spacing accessing the liquid phase in the  $(1\bar{1}01)$  orientation. The layer spacing of  $(1\bar{1}01)$  interfaces finally approaches to (0001), reaching same value before the peaks decay in the liquid phase.

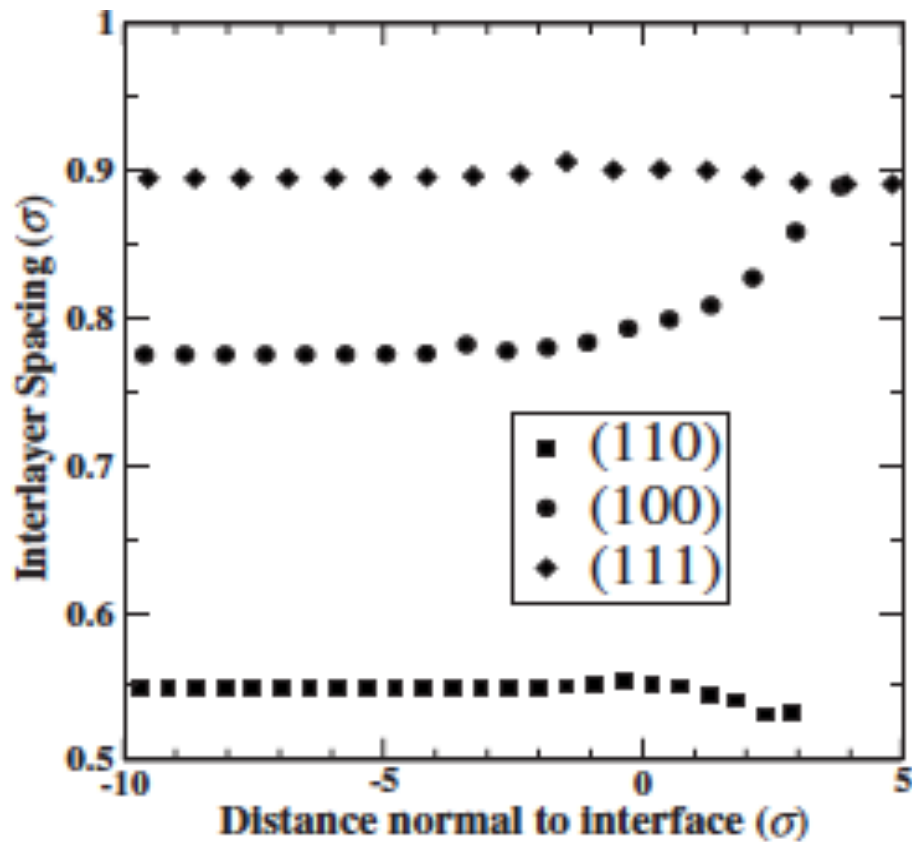


Fig 4.5: The interplanar spacing as a function of distance normal to the interface for the FCC (100), (110), and (111) LJ solid-liquid interfaces in LJ reduced unit [41]

The spacing of  $(11\bar{2}0)$  interface also exhibits a slight expansion, but in most cases, maintains its layer distance into the liquid. These results of HCP Mg show exactly the same trend to that obtained in previous studies on FCC [41, 42, 116, 117] crystal-melt systems. This relevant phenomenon also from another side proves our simulation is reasonably performed. As mentioned in the last of section 4.1.1.1, this anisotropy of layer spacing variation in HCP Mg also can be viewed as a possible support of the assumption about anisotropy of structural widths by Broughton and Gilmer [117], since in HCP Mg

layer spacing of  $(1\bar{1}01)$  expands to that of  $(0001)$  while layer spacing of  $(11\bar{2}0)$  is much less than that of  $(0001)$  and  $(1\bar{1}01)$  interfaces. If the fluid structure factor  $S(q)$  of the HCP is also close to the layer spacing of most compact interface  $(0001)$ , that fact shown in the Fig. 4.1-4.3 that the density oscillations of  $(0001)$  and  $(1\bar{1}01)$  can spread longer in the liquid with lowest energy cost, will follow that assumption. Thus, this phenomenon of layer separation in HCP Mg can be regarded as a partially support of that assumption about anisotropy of structural widths.

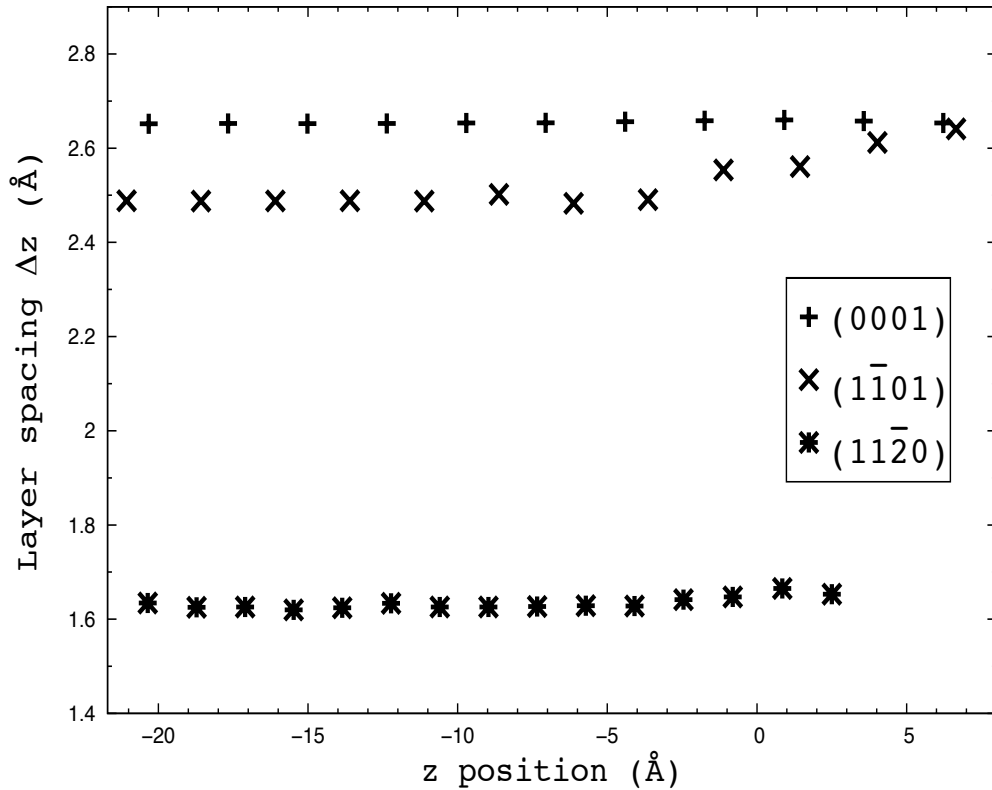


Fig. 4.6: Layer spacing variations with the direction along interface normal for three interfaces.

### 4.1.3 Stress Profiles and Their Anisotropy

Interfacial stress profiles plotted for the three interfaces are shown in Fig. 4.7. The results are analyzed with calculated standard error, where the error bars denote the 95% confidence limit. An integration of the stress profile including interfacial region gives the interfacial stress  $\tau$  according to equation 2.19 and all interfacial stresses for three interfaces are listed in Table 4.2. It is clear that for all of these low index orientations the interfacial stress is negative, representing a state of compression. The (0001) interface has the largest absolute value and (1 $\bar{1}$ 01) has the smallest, while (11 $\bar{2}$ 0) lies in between. With the predetermined value of interfacial free energy  $\gamma$  from the work by Sun et al. [16], listed in Table 4.2, we can easily conclude that the interfacial stress has the same magnitude as interfacial free energy for the (0001) interface, with a  $\tau/\gamma$  ratio of almost 1.0, whereas the (1 $\bar{1}$ 01) interface has a  $\tau/\gamma$  ratio of almost 0.5. Since it is mentioned previously that (0001), (1 $\bar{1}$ 01) and (11 $\bar{2}$ 0) interfaces in the HCP are comparable with (111), (100) and (110) interfaces respectively according density of interfaces and previous corresponding results, it is reasonable to compare the  $\tau/\gamma$  ratio with previous works of FCC systems: For the LJ systems of Laird et al. [41] and Broughton and Gilmer [117], the  $\tau/\gamma$  ratio for the FCC (111) interface, identical with (0001) in the HCP, is around 2.0; For hard sphere system of Davidchack and Laird [46] the  $\tau/\gamma$  ratio for (111) is around 1.2; For an elemental Ni system with a description of EAM potential of work of Becker et al. [77], the  $\tau/\gamma$  ratio for the FCC (100), identical with (1 $\bar{1}$ 01) in the HCP, is around 0.24-0.53; For Broughton and Gilmer [117], the  $\tau/\gamma$  ratio for (100) is also about 0.5. From the

comparison above, the trend of  $\tau/\gamma$  ratio seems in a reasonable range. However, although  $\tau$  values from mentioned systems are always have the negatives values, there are exceptions. In the simulation of silicon system with description of Stilling-Weber potential [77], the interfacial stresses  $\tau$  are positive both in (111) and (100) interfaces. The reason for this is still open to research. It might be related to special conditions of density difference between solid and liquid in silicon system, because, unlike general metal systems, the silicon has a larger density in liquid than in crystal.

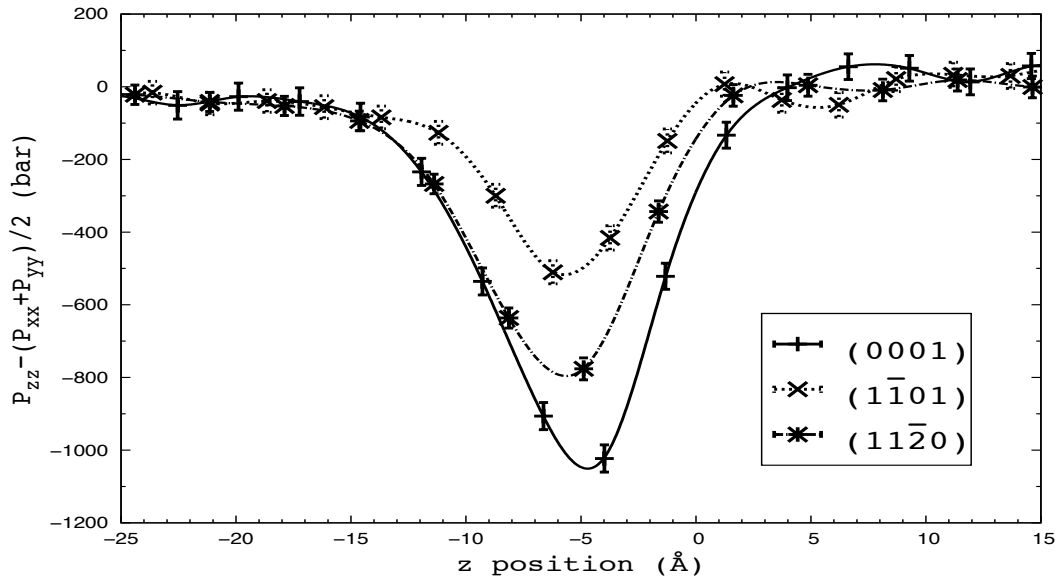


Fig. 4.7: Interfacial stress profiles along the interface normal for all three directions.

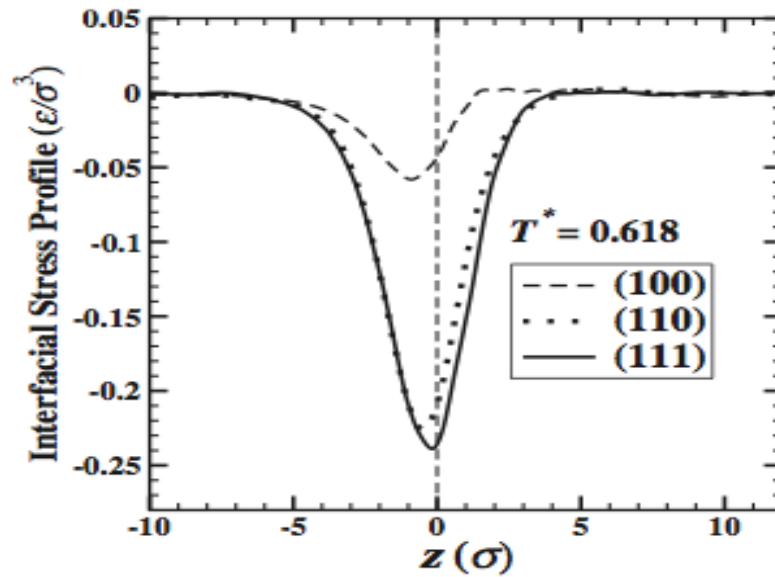


Fig. 4.8: Interfacial stress profiles for the LJ crystal-melt interface at equilibrium temperature for (111), (100) and (111) interfaces [41].

In the sequence of values of interfacial stress of three interfaces, the interesting thing is that we found not only they exhibit a fairly larger anisotropy than interfacial free energy, but also the sequence itself is very special. It is special because anisotropy of interfacial stress profiles does not follow the order of compact planes shown in fine-grained density profiles like in our previous results of investigation. Moreover, this special situation was also found in the FCC LJ system in works of Broughton and Gilmer [117] and Laird et al. [41] as shown Fig. 4.8, in which (100) interface, identical with  $(\bar{1}101)$  in the HCP, took the least value of  $\tau$  in magnitude. In their works, they pointed out that (100) was special but hadn't offered an explanation for this specialty, more especially for the strange sequence of anisotropy of interfacial stresses. In our work, we try to

explore more of this interesting phenomenon by relating it to the interesting expansion of interlayer spacing of  $(1\bar{1}01)$  interface in the HCP, which behaves similarly with the comparable  $(100)$  interface in the FCC. Inspired by the research on simulation of crystal growth from its melt by Huitema et al. [83], we have drawn a figure of occupation fraction versus  $z$  direction as in Fig. 4.8. Occupation fraction,  $N_i/N_c$ , is defined as the number of particles per layer  $N_i$  divided by that in the bulk crystal  $N_c$ . Generally from fine-grained density profiles (see Fig. 4.1-4.3), the peak values of fine-grained densities  $\rho(z^{peak})$  are decreasing across the interfacial region. Because the interlayer spacing of both  $(0001)$  and  $(11\bar{2}0)$  mainly remain constant with negligible variation (Fig. 4.6), it is natural to imagine that the layer occupation fractions of the two interfaces decrease across the region as shown in Fig. 4.9. On the other hand, in  $(1\bar{1}01)$  interface, even the peak values of density in fine-grained density  $\rho(z^{peak})$  decrease as well. The expansion of layer spacing  $\Delta z$  across the  $(1\bar{1}01)$  interface may effectively impede the total decrease of its occupation fraction. As observed in Fig. 4.9, the occupation fraction  $N_i/N_c$  of  $(1\bar{1}01)$  interface only slightly decreases. The trend of  $(1\bar{1}01)$  profile in the Fig. 4.9 almost maintains flat across the interfacial region, compared with both  $(0001)$  and  $(11\bar{2}0)$  interfaces both dropping dramatically.

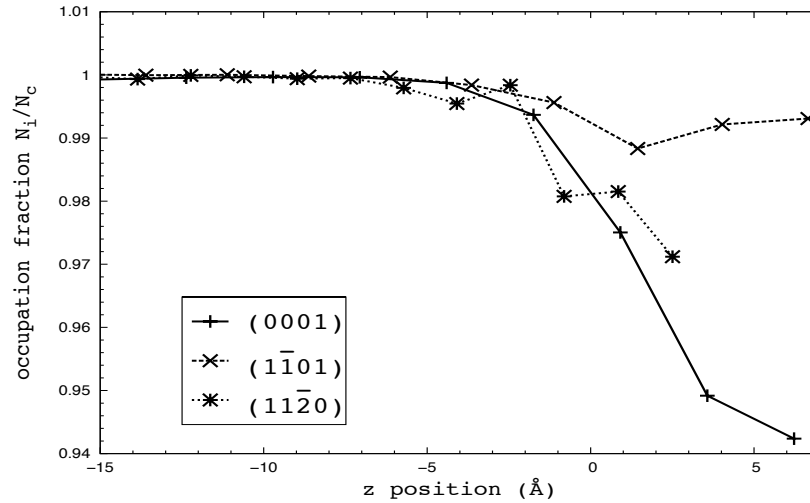


Fig. 4.9: Occupation fraction profiles  $N_i/N_c$  along  $z$  direction for all three interfaces.

Occupation fraction is defined as the number of particles per layer  $N_i$ , through the interface region where the layer still can be clearly recognized, divided by that per layer  $N_c$  in the bulk crystal.

Moreover, the same trend of this occupation fraction profiles with comparable interfaces in the FCC structure also can be found in Huitema et al. [116] in Fig. 4.10, in which the occupation fraction of (100) interface has shown little decrease while (111) and (110) showed the otherwise. Thus it is exciting that in Huitema's study, the anisotropy of occupation fraction profiles followed exactly the same order as that of correspondent interfacial stress profile in Laird et al. [41] in Fig.4.8 and this correlation in FCC systems consequently support our correspondent results in the HCP structure.

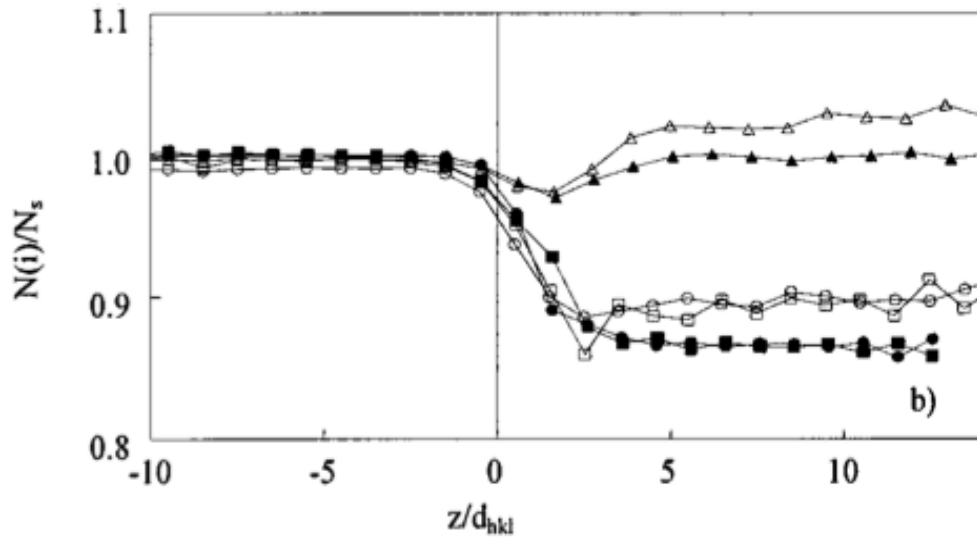


Fig. 4.10: Occupation fraction,  $N_i/N_c$ , as function of position for three interfaces across the solid-liquid interface with Lennard Jones potential at its equilibrium temperature 72K (solid points) and a lower temperature 60K (hallow points), (111) interface is plotted in circles, (100) plotted in triangles and (110) plotted in squares [116].

In summary, at the premise of a system with larger density in crystal than in liquid, this special anisotropy of interfacial stress  $\tau$  in metal system is highly related to, even follows, the trend of correspondent occupation fraction profiles, which have incorporated the characteristics of interlayer expansions with different interfaces. And this correlation has been proven in the HCP structure with EAM potential in our simulation as well as in the FCC structure with the LJ potential [41, 116]. The answer for this correlation possibly can be, the steeper slopes of variation in layer density (or occupation fraction), the higher absolute values of interfacial stresses.

## 4.2 Temperature Dependence of $\gamma$ at Non-equilibrium Temperatures

To study the temperature dependence of  $\gamma$ , we choose four more temperatures below the melting temperature  $T_M$ : 550K, 700K, 800K and 860K. As mentioned in Chapter two, we will use Gibbs-Cahn integration technique to derive the dependence of interfacial free energy  $\gamma$ . However, we have to make the simplifying assumption that at other selected temperatures, both excess energy  $e$  and interfacial stress  $\tau$  remain constant at the values obtained at  $T_M$ , since they can only easily be obtained from direct MD simulations under equilibrium condition. It is important to note that we are interested in the temperature dependence of  $\gamma$  at constant pressure ( $P=0$ ), therefore the temperature dependence of  $e$  and  $\tau$  cannot be easily determined because a stable crystal-melt interface cannot be formed at those non-equilibrium temperatures. For a computation of the temperature dependence of the excess interfacial free energy along the solid-liquid coexistence line, reader is recommended to refer to the work of Laird et al. [41]. In our simulation, the computed excess energy  $e$  and excess entropy  $\eta$  are presented in Table 4.2, in which the error bars represent the standard errors with 95% confidence interval. It is very obvious from Table 4.2, that excess energy  $e$ , interfacial stress  $\tau$  and excess entropy  $\eta$  are much more anisotropic than interfacial free energy  $\gamma$ , in which special anisotropy of  $\tau$  has been discussed. Besides, anisotropies of  $e$ ,  $\eta$  and  $\gamma$  at melting temperature all follow the order of compact planes.

TABLE 4.2 Excess energy  $e$ , interfacial stress  $\tau$  and excess entropy  $\eta$  calculated at melting temperature.

Interface	(0001)	(1 $\bar{1}$ 01)	(11 $\bar{2}$ 0)
$e$ (mJ/m <sup>2</sup> )	62.1±11.9	31.2±14.1	22.9±15.2
$\tau$ (mJ/m <sup>2</sup> )	-89.9±4.9	-44.0±4.1	-75.2±4.9
$\eta$ (mJ/(m <sup>2</sup> K))	-0.029±0.013	-0.065±0.016	-0.075±0.017
$\gamma^1$ (mJ/m <sup>2</sup> )	88.4±1.7 <sup>1</sup>	90.1±1.5 <sup>1</sup>	90.8±1.6 <sup>1</sup>

<sup>1</sup>Reference 16

TABLE 4.3. Bulk solid density at chosen temp and bulk solid and liquid number and energy densities at  $T_M$ .

	911K	860K	800K	700K	550K
$\rho_s$ (nm <sup>-3</sup> )	41.1687(1)	41.3941(2)	41.6350(2)	41.9935(2)	42.4617(2)
$\rho_l$ (nm <sup>-3</sup> )	38.9034(5)				
$\rho_s^E$ (eV/nm <sup>3</sup> )	-56.9522(3)				
$\rho_l^E$ (eV/nm <sup>3</sup> )	-49.9313(7)				

Besides  $e$ ,  $\tau$  and  $\rho_s$  at selected temperatures in Table 4.2 and 4.3, we still need to get  $d\rho_s/dT$  term in equation 2.33 at zero pressure in order to obtain right hand side of the equation. The first step is to get  $\rho_s$  as a function of temperature  $T$  by fitting  $\rho_s$  to listed

temperatures via a polynomial fit. Then it is taken first order derivative to  $T$  to obtain  $d\rho_s/dT$ . The result of the calculation in our simulation can be expressed:

$$\frac{d\rho_s}{dT} = -2.1063E-004 - 4.5974E-006 \cdot T. \quad (4.1)$$

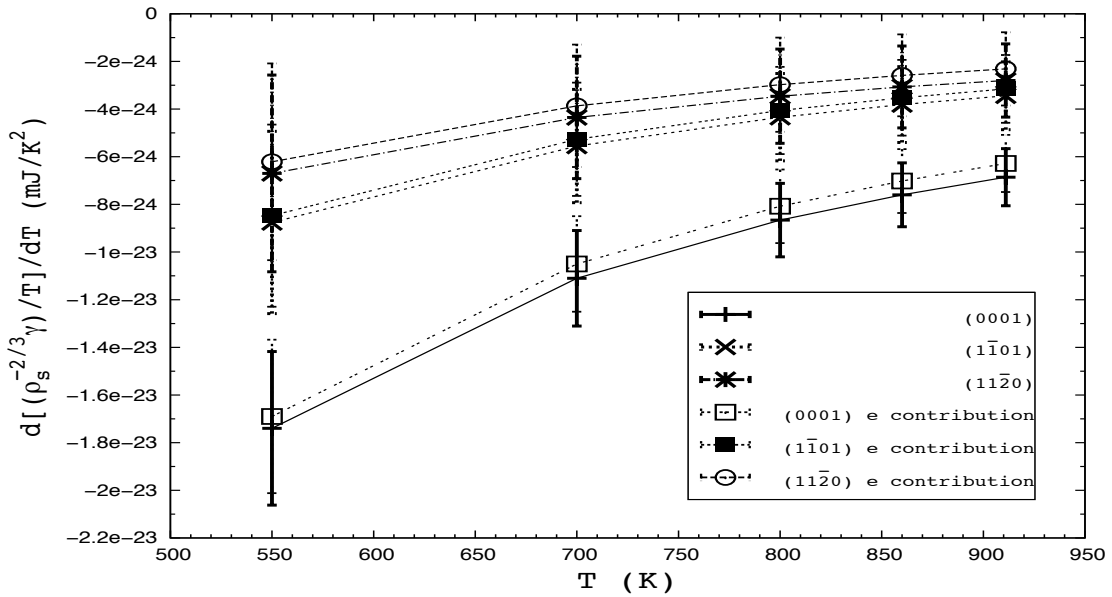


Fig. 4.11: The integrand of equation 2.33,  $d[(\rho^{-2/3}Y)/T]/dT$ , varying with temperature for all three interfaces. The total values and the partial values contributed by excess energy  $e$  are plotted respectively.

Based on the previous information, the right hand side of the equation 2.33, the integrand before final integration, can be calculated as a function of selected temperature  $T$ . The results are shown in Fig 4.11. From equation 2.33, we could clearly observe that the integrand consists of two parts: one related to  $e$  and other related to  $\tau$ . Thus, in this figure, we have plotted total integrands as well as the partial contributions only from  $e$ .

The figure shows that  $e$  terms for three interfaces all takes up the main value of the integrand. Thus the value of  $e$  is more important in this calculation and the accuracy of the final integration of  $\gamma$  can be more sensitive to the standard error of  $e$  values than that of the other factor  $\tau$ .

TABLE 4.4:  $\gamma$  under non-equilibrium condition at selected temperatures.

	550K	700K	800K	860K
$\gamma(0001)$ (mJ/m <sup>2</sup> )	81.1±2.4	84.4±1.8	86.5±1.7	87.6±1.7
$\gamma(1\bar{1}01)$ (mJ/m <sup>2</sup> )	68.9±2.7	77.9±1.9	83.8±1.6	87.2±1.5
$\gamma(11\bar{2}0)$ (mJ/m <sup>2</sup> )	66.4±2.9	76.9±2.0	83.7±1.7	87.6±1.6

With integrand  $d[(\rho_s^{-2/3}\gamma)/T]/dT$  obtained, now we can integrate the equation 2.33, employing trapezoid rule and starting from  $\gamma$  at  $T_M$ , that have already been calculated [17] and listed in Table 4.4 to obtain other  $\gamma$  at non-equilibrium temperatures. The values of  $\gamma$  at selected non-equilibrium temperatures are calculated and listed in Table 4.4 as well as are plotted in Fig. 4.12.

Our estimation of temperature dependence of interfacial free energy  $\gamma$  at non-equilibrium temperatures is clearly shown in the Fig. 4.12. As described in this figure, at non-equilibrium temperatures, the  $\gamma$  linearly increases with temperature  $T$  and reaches the highest value for each of three interfaces at the melting point  $T_M$ . This situation is similar to the results at coexistent line under equilibrium temperature of the LJ system from the

work of Laird et al. [41]. In their investigation, although under equilibrium at all temperatures, the interfacial free energies increase with temperature for all three interfaces, (111), (100) and (110). However, more specifically in our system, at non-equilibrium temperatures, the interfacial free energy  $\gamma$  experiences a linear increase with temperatures until reaching the melting point for each of the three interfaces, (0001), ( $1\bar{1}01$ ) and ( $11\bar{2}0$ ).

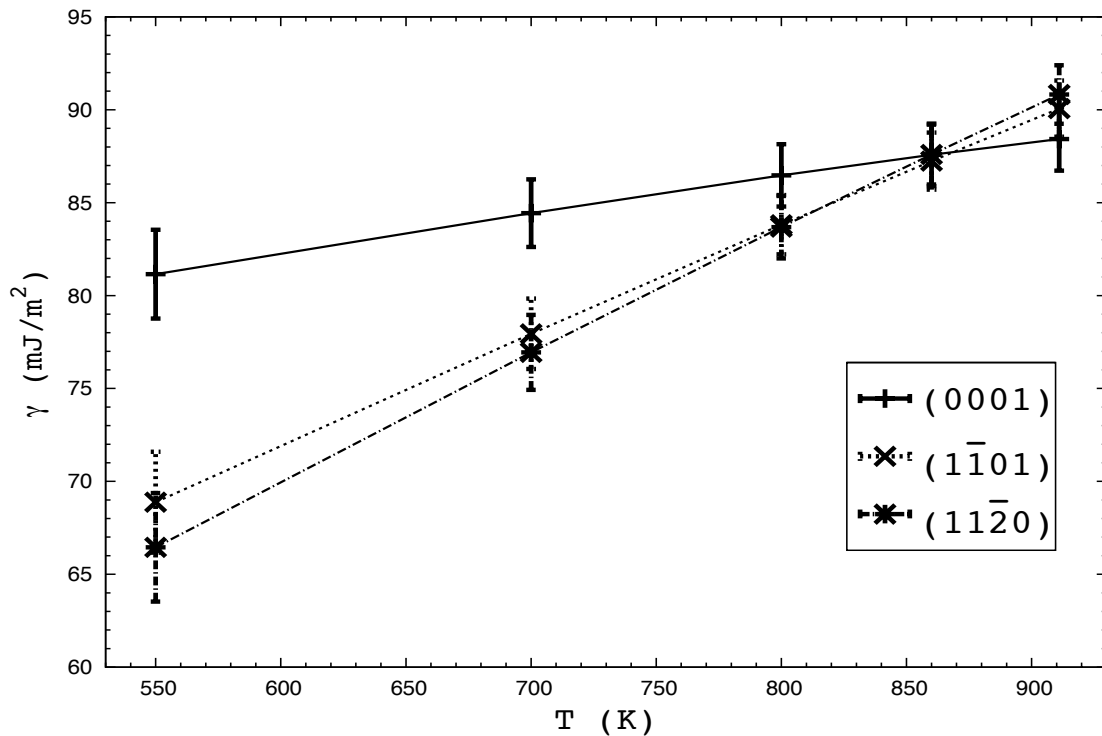


Fig. 4.12: Temperature dependence of  $\gamma$  for the three interfaces under non-equilibrium temperatures until the melting point  $T_M$

More specifically, at the melting point,  $\gamma$  of  $(11\bar{2}0)$  interface has the highest value and  $(0001)$  is the most stable interface with lowest value. However, when temperature begins to decrease, the  $\gamma$  value of  $(11\bar{2}0)$  decreases with largest decreasing ratio, while that of  $(0001)$  holds the lowest decreasing ratio. Finally, at our lowest selected non-equilibrium temperature 550K, it becomes to be obvious that  $\gamma$  of  $(11\bar{2}0)$  and  $(1\bar{1}01)$  are much lower than that of the most stable interface  $(0001)$  at the melting temperature. The above characteristics about temperature dependence of  $\gamma$  at non-equilibrium temperatures are very interesting but still cannot be clearly explained yet. If these interesting simulation results can be more accurately proved by other methods or theories, they would be more convincing and very meaningful.

The anisotropy of interfacial free energy  $\gamma$  can be important in solidification processes. As known in thermodynamics of transformation, the interface with a lower interfacial free energy is more easily nucleated with and will likely possess larger interfacial area during the solidification process to lower down the total energy of the system. This effect on solidification process will possibly have an impact on the final product.

Thus the anisotropy of interfacial free energy at different non-equilibrium temperatures can be important as well. If the results are more conceivably proved in the future, we can employ this dependent relationship to obtain desired products by controlling the anisotropy of interfacial free energy  $\gamma$  via different temperatures in commonly used solidification processes at non-equilibrium temperatures.

## CHAPTER FIVE

### FUTURE RESEARCH

---

As a detailed investigation of molecule dynamics simulation of HCP Mg, some suggestions are proposed for the future work and summarized as follows:

1. In the context of supporting the hypothesis proposed by Broughton and Gilmer [117] to explain the anisotropy of structural widths in HCP Mg, the liquid structure factor  $S(q)$  for our Mg system needs to be calculated to confirm this explanation.
2. In the study of interfacial stress, although most previous studies reported a negative value,  $\tau$  is positive in the silicon system described using the Stillinger-Weber potential [77]. It has been proposed that the positive value of  $\tau$  is because the density of crystal Si is lower than that of liquid, but the real answer is still unclear and open to further investigation.
3. In Table 4.2, other than  $\tau$ , the fact that the anisotropy of excess energy  $e$ , excess entropy  $\eta$  and interfacial free energy  $\gamma$  follows the order of density of interfaces, implying some possible relation between them. The information about this issue is still unknown and open for future research.
4. In our estimation of temperature dependence of  $\gamma$  at non-equilibrium temperatures, we use the value of  $e$  and  $\tau$  at the melting temperature to estimate

the values at the non-equilibrium temperatures. These assumptions decrease the accuracy in the thermodynamic integration and thus reduces the reliability of the results. If we can employ some other method or theory in the future to obtain more accurate values of excess energy  $e$  and interfacial stress  $\tau$  at the corresponding temperatures, the thermodynamic integration and its subsequent result about interfacial free energy will be more reliable and useful.

## CHAPTER SIX

## CONCLUSION

---

Through molecular dynamics simulations study of solid-liquid interfaces in HCP elemental Mg of three representative orientations (0001),  $(1\bar{1}01)$  and  $(11\bar{2}0)$ , structural and thermodynamic properties have been investigated. After the simulated Mg system has been characterized by the important structural and thermodynamic methods we have chosen, the conclusions that have been draw from this investigation are summarized in the following:

1. The structural properties investigated in this work are: the interfacial widths, the interlayer spacing variation and the interfacial stress profile. The structural widths of three interfacial orientations, defined by fine-grained density, show obvious anisotropy. It can be possibly explained by the hypothesis proposed by Broughton and Gilmer [117], if the fluid structure factor  $S(q)$  of Mg simulation system is close to the interlayer spacing of (0001) interface.
2. The intrinsic width mainly describes the 10-90 width from coarse-grained density profiles and is widely used to define the width of an interfacial region. These important data from HCP Mg of our three interfacial orientations are roughly  $8 \text{ \AA}$  or  $3\sigma$  with very weak anisotropy, while the structural widths have values of about

16 Å, almost twice of intrinsic widths. These results are compared with previous MD studies on FCC systems and they are within a similar range of values.

3. The anisotropy of interlayer spacing variation is a very interesting and important phenomenon as it shows the structural variation across a crystal-melt interface region for different interfaces. This anisotropy of variation is also observed in our simulation of Mg system and can be comparable with that in an FCC system.
4. There is a special anisotropy associated with the stress profiles, which has not been explained before in any systems. Inspired by the work of Huitema et al. [116], we propose to use occupation fraction profiles to try to probe it. The anisotropy of the occupation fraction profiles is similar to the anisotropy of interfacial stress profiles in our simulation of Mg as well as in the FCC LJ system.
5. Since interfacial free energy  $\gamma$  of HCP Mg has been calculated and the temperature dependence of  $\gamma$  in the FCC LJ system has been studied, our purpose of study on thermodynamic properties is then shifted to an estimation of temperature dependence of interfacial free energy  $\gamma$  at non-equilibrium temperatures by the thermodynamic integration technique. Through the calculation of excess energy  $e$  contribution to the integrand, the accuracy of the final integration is found to be more sensitive to the standard error of  $e$  values than that of the interfacial stress  $\tau$ .
6. After the thermodynamic integration, an increase of  $\gamma$  with increasing temperature is found in all three interfaces. The values of  $\gamma$  of  $(11\bar{2}0)$  and  $(1\bar{1}01)$  interfaces

increase with a greater ratio than that of (0001) interface. The FCC LJ system under equilibrium condition [41] shares the similar increasing except for the linear relation. If further investigation can accurately prove this estimation, we could then employ this dependent relationship to obtain desired products by controlling the anisotropy of interfacial free energy  $\gamma$  via different temperatures in common solidification processes at non-equilibrium temperatures.

## References

- [1] Tiller W.A., *The Science of Crystallization: Microscopic Interfacial Phenomena*, Cambridge University Press, New York, 1991.
- [2] Boettinger W.J., Coriell S.R., Greer A.L., Karma A., Kurz W., Rappaz M., and Trivedi R., *Acta Mater*, 2000, vol. 48, pp. 43.
- [3] Nam H. and Srolovitz D.J., *Phys Rev. B*, 2007, vol. 76, pp. 184114.
- [4] Adamson A.W. and Gast A.P., *Physical Chemistry of Surfaces*, Wiley-Interscience, New York, 1997.
- [5] Glicksman M.E., Vold, C., *Acta Metall.* 1969, vol. 17, pp. 1.
- [6] Hardy S.C., *Philos. Mag.*, 1977, vol. 35, pp. 471.
- [7] Schaefer R.J., Glicksman M.E., Ayere J.D., *Philos. Mag.*, 1975, vol. 32, pp. 725.
- [8] Mutaftchiev B., Zell J., *Surf. Sci.*, 1968, vol. 12, pp. 317.
- [9] Grange G., Landers R., Mutaftchiev B.J., *Crystal Growth*, 1980, vol. 49, pp. 343.
- [10] Turnbull D.J., *Appl. Phys.*, 1950, vol. 21, pp. 1022.
- [11] Woodruff D.P., *The Solid–Liquid Interface*, Cambridge University Press, London, 1973.
- [12] Howe J.M., *Philos. Mag. A*, 1996, vol. 74, pp. 761.
- [13] Alder, B.J. and Wainwright T.E., "Studies in Molecular Dynamics. I. General Method". *J. Chem. Phys.*, 1959, vol. 31, no. 2, pp. 459.

- [14] Berg B.A., *Markov Chain Monte Carlo Simulations and Their Statistical Analysis (With Web-Based Fortran Code)*, World Scientific, Hackensack, NJ, 2004.
- [15] Lide D.R., *CRC Handbook of Chemistry and Physics*, vol. 4, CRC Press, New York, 2007.
- [16] Liu X.Y., Adams J.B., Ercolessi F. and Moriarty J.A., *MSMSE*, 1996, vol. 4, pp. 293.
- [17] Sun D.Y., Mendeleev M.I., Becker C.A., Kudin K., Haxhimali T., Asta M., Hoyt J.J., Karma A. and Srolovitz D.J., *Phys. Rev. B*, 2006, vol. 73, pp. 024116.
- [18] Xia Z.G., Sun D.Y., Asta M. and Hoyt J. J., *Phys. Rev. B*, 2007, vol. 75, pp. 012103.
- [19] Gao Y.F., Yang Y., Sun D.Y., Asta M. and Hoyt J.J., *Journal of Crystal Growth*, 2010, vol. 312, pp. 3238–3242.
- [20] Tang T., Kim S. and Horstemeyer M.F., *Computational Materials Science*, 2010, vol. 48, pp. 426–439.
- [21] Yasi J.A., Nogaret T., Trinkle D.R., Qi Y., Hector Jr. L.G. and Curtin W.A., *Modelling Simul. Mater. Sci. Eng.*, 2009, vol. 17, pp. 055012.
- [22] Groh S., Marin E.B., Horstemeyer M.F. and Bammann D.J., *Modelling Simul. Mater. Sci. Eng.*, 2009, vol. 17, pp. 075009.
- [23] Wang M., Jing T. and Liu B., *Scripta Materialia*, 2009, vol. 61, pp. 777–780.
- [24] Eiken J., *Materials Science Forum*, 2010, vol. 649, pp. 199-204.
- [25] Hoover W.G., Gray S.G. and Johnson K.W.J., *Chem. Phys.*, 1971, vol. 55, pp. 1128.
- [26] Laird B.B. and Haymet A.D.J., *Mol. Phys.*, 1992, vol. 75, pp. 71.
- [27] Ladd A.J.C. and Woodcock L.V., *Chem. Phys. Lett.*, 1977, vol. 51, pp. 155.
- [28] Laird B.B., Haymet A.D.J., *Chem. Phys.*, 1989, vol. 91, pp. 3638.

- [29] Broughton J.Q., Bonnissent A. and Abraham F.F.J., *Chem. Phys.*, 1981, vol. 74, pp. 4029.
- [30] Broughton J.Q. and Gilmer G.H., *Acta Metall.*, 1983, vol. 31, pp. 845.
- [31] Broughton J.Q. and Gilmer G. H., *Chem. Phys.*, 1986, vol. 84, pp. 5759.
- [32] Bonnissent A. and Mutaftschiev B., *Philos. Mag.*, 1977, vol. 35, pp. 65.
- [33] Tallon J., *Phys. Rev. Lett.*, 1986, vol. 57, pp. 1328.
- [34] Toxvaerd S. and Praestgaard E.J., *Chem. Phys.*, 1977, vol. 67, pp. 5291.
- [35] Broughton J.Q. and Abraham F. F., *Chem. Phys. Lett.*, 1980, vol. 71, pp. 456.
- [36] Landman U., Barnett R.N., Cleveland C.L. and Ut R.H.J., *Vac. Sci. Technol.*, 1984, vol. A3, pp. 1574.
- [37] Broughton J.Q. and Gilmer G.H.J., *Chem. Phys.*, 1986, vol. 84, pp. 5759.
- [38] Galejs R.J., Ravech H.J. and Lie G., *Phys. Rev. A*, 1989, vol. 39, pp. 2574.
- [39] Kyrlidis A. and Brown R.A., *Phys. Rev. E*, 1995, vol. 51, pp. 5832.
- [40] Mori A., Manabe R. and Nishioka K., *Phys. Rev. E*, 1995, vol. 51, pp. 3831.
- [41] Laird B.B., Davidchack R.L., Yang Y. and Asta M., *J. Chem. Phys.* 2009, vol. 131, pp. 114110.
- [42] Davidchack R.L. and Laird B.B., *J. Chem. Phys.*, June 1998, vol. 108, no. 22, pp. 8.
- [43] Buehnell-Wye G., Finney J.L. and Bonnissent A., *Philos. Mag.*, 1981, vol. 44, pp. 1053.
- [44] Laird B.B. and Haymet A.D.J., *Materials Research Society Symposia Proceedings*, 1986, vol. 63, pp. 67-72.

- [45] Gibbs J.W., *The Collected Works*, vol. 1, Yale University Press, New Haven, CT, 1957.
- [46] Davidchack R.L. and Laird B.B., *Phys. Rev. Lett.*, 2000, vol. 85, pp. 4751.
- [47] Hoyt J. J., Asta M., and Karma A., *Phys. Rev. Lett.*, 2001, vol. 86, pp. 5530.
- [48] Cahn J.W., *Interfacial Segregation*, edited by Johnson W.C. and Blakely J.M., American Society for Metals, Metals Park, OH, 1979, pp. 3–23.
- [49] Frolov T. and Mishin Y., *Phys. Rev. B*, 2009, vol. 79, pp. 045430.
- [50] Frolov T. and Mishin Y., *J. Chem. Phys.*, 2009, vol. 131, pp. 054702.
- [51] Frenkel D. and Smit B., *Understanding Molecular Simulation: From Algorithms to Applications*, Academic Press, San Diego, 1996.
- [52] Maitland G.C., Rigby M., Smith E.B., and Wakeham W.A., *Intermolecular forces: their origin and determination*, Clarendon Press, Oxford, 1981.
- [53] Jones J.E., *Proc. R. Soc. Lond. A*, 1924, vol. 106, no. 738, pp. 463-477.
- [54] Weeks J., Chandler D. and Andersen H.C., *J. Chem. Phys.*, 1971, vol. 54, pp. 5237-5247.
- [55] Allen M.P., *Introduction to Molecular Dynamics Simulation*, NIC Series, 2004, vol. 23, pp. 1-28.
- [56] Daw M.S. and Baskes M.I., *Physical Review B*, 1984, vol. 29, no. 12, pp. 6443-6453.
- [57] Johnson R. A., *Physical Review B*, 1972, vol. 6, pp. 2094.
- [58] Oh D.J., and Johnson R.A., *J. Mater. Res.*, 1988, vol. 3, pp. 471.
- [59] Igarashi M., Kanta K. and Vitek V., *Phil. Mag. B*, 1991, vol. 63, pp. 603.
- [60] Pasianot R. and Savino E.J., *Physical Review B*, 1992, vol. 45, pp. 12704.

- [61] Baskes M.I., and Johnson R.A., *Modeling Simulation Mater. Sic. Eng.*, 1994, vol. 2, pp. 147.
- [62] Baskes M.I., *Phys. Rev. Lett.*, 1987, vol. 59, pp. 2666.
- [63] Voter A.F. and Chen S.P., *Mater. Res. Soc. Symp. Proc.*, 1987, vol. 82, pp.175.
- [64] Ercolessi F. and Adam J. B., *Europhys. Lett.*, 1994, vol. 26, pp. 583.
- [65] Efimov A.I., Belorukova L.P., Vasilkova I.V. and Chechev V.P., *Properties of Inorganic Compounds (in Russian)*, Khimiya, Leningrad, 1983.
- [66] Moriaty J.A. and Althoff J.D., *Physical Review B*, 1995, vol. 51, pp. 5609.
- [67] Sturgeon J. B. and Laird B. B., *Physical Review B*, 2000, vol. 62, pp. 14720.
- [68] Finkelstein R. J., *Thermodynamics and Statistical Physics*, Freeman W. H., San Francisco, 1970.
- [69] Landau L.D. and Lifshitz, E.M., *Statistical Physics. Pergamon Press.*, 1980, pp. 9.
- [70] Yang Y., Humadi H., Buta D., Laird B.B., Sun D., Hoyt J.J., and Asta M., *Phys. Rev. Lett.*, 2011, vol. 107, pp. 025505.
- [71] Morris J.R. and Lu Z.Y., Ye Y.Y. and Ho K.M., *Interface Science*, 2002, vol. 10, pp. 143–148.
- [72] Steinhardt P.J., Nelson D.R., and Ronchetti M., *Phys. Rev. B*, 1983, vol. 28, pp. 784.
- [73] Rodriguez O.F. and Soler J.M., *Phys. Rev. Lett.*, 1998, vol. 81, pp. 3159.
- [74] Briels W.J. and Tepper H.L., *Phys. Rev. Lett.*, 1997, vol. 79, pp. 5074.
- [75] Press W.H., Teukolsky S.A., Vetterling W.T., and Flannery B.P., *Numerical Recipes in Fortran*, 2nd ed., Cambridge University Press, Cambridge, 1992.

- [76] Shuttleworth R., *Proc. Phys. Soc., London, Sect. A*, 1949, vol. 63, pp. 444.
- [77] Becker C.A., Hoyt J.J., Buta D. and Asta M., *Physical Review E*, 2007, vol. 75, pp. 061610.
- [78] Plimpton S., *Comput. Phys.*, 1995, vol. 117, pp. 1–19.
- [79] Glicksman M.E. and Vold C.L., *Scr. Metall.*, 1971, vol. 5, pp. 493.
- [80] Eustathopoulos N., *Intl. Met. Rev.*, 1983, vol. 28, pp. 189.
- [81] Napolitano R.E. and Liu S., *R. Trivedi, Interf. Sci.*, 2002, vol. 10, pp. 217.
- [82] Browner R., Kessler D., Koplik J., and Levine H., *Phys. Rev. Lett.*, 1983, vol. 51, pp. 1111.
- [83] Kessler D., Koplik J., and Levine H., *Phys. Rev. A*, 1984, vol. 29, pp. 3161.
- [84] Kessler D. and Levine H., *Phys. Rev. Lett.*, 1986, vol. 57, pp. 3069.
- [85] Langer J.S., *Phys. Rev. A*, 1986, vol. 33, pp. 435.
- [86] Langer J.S., *Phys. Rev. A*, 1989, vol. 39, pp. 5314.
- [87] Akamatsu S., Faivre G., and Ihle T., *Phys. Rev. E*, 1995, vol. 51, pp. 4751.
- [88] Kobayashi R., *Physica D*, 1993, vol. 63, pp. 410.
- [89] Wang S. and Sekerka R., *Phys. Rev. E*, 1996, vol. 53, pp. 3760–3776.
- [90] Karma A. and Rappel W., *Phys. Rev. E*, 1998, vol. 57, pp. 4323,
- [91] Huang S.C. and Glicksman M.E., *Acta Metall.*, 1981, vol. 29, pp. 701.
- [92] Glicksman M.E. and Singh N.B., *J. Cryst. Growth*, 1989, vol. 98, pp. 277.
- [93] Muschol M., Liu D., Cummins H.Z., *Phys. Rev. A*, 1992, vol. 46, pp. 1038.
- [94] Liu S., Napolitano R.E. and Trivedi R., *Acta Mater.*, 2001, vol. 49, pp. 4271.
- [95] Turnbull D., *J. Chem. Phys.*, 1952, vol. 20, pp. 411.

- [96] Spaepen F., *Solid State Phys.*, 1994, vol. 47, pp. 1.
- [97] Skapski A.S., *Acta Metall.*, 1956, vol. 4, pp. 576.
- [98] Ewing R.H., *J. Cryst. Growth*, 1971, vol. 11, pp. 221.
- [99] Waseda Y. and Miller W.A., *Trans. Jpn. Inst. Met.*, 1978, vol. 19, pp. 546.
- [100] Miedema A.R. and den Broeder F.J.A., *Z. Metallkd.*, 1979, vol. 70, pp. 14.
- [101] Granasy L., *J. Non-Cryst. Solids*, 1993, vol. 162, pp. 301.
- [102] Jian Z.Y., Kuribayashi K. and Jie W.Q., *Mat. Trans.*, 2002, vol. 43, pp. 721.
- [103] Spaepen F., *Acta Metall.*, 1975, vol. 23, pp. 729.
- [104] Spaepen F. and Meyer R.B., *Scripta Metall.*, 1976, vol. 10, pp. 257.
- [105] Nelson D.R. and Spaepen F., *Solid State Phys.*, 1989, vol. 42, pp. 190.
- [106] Spaepen F., *Mat. Sci. Eng. A*, 1994, vol. 178, pp. 15.
- [107] Bonnissent A., Finney J.L., Mutaftschiev B., *Philos. Mag. B*, 1980, vol. 42, pp. 233.
- [108] Curtin W.A., *Phys. Rev. Lett.*, 1987, vol. 59, pp. 1228.
- [109] Curtin W.A., *Phys. Rev. B*, 1989, vol. 39, pp. 6775.
- [110] Laird B.B., *J. Chem. Phys.*, 2001, vol. 115, pp. 2887.
- [111] Miyazawa Y., Pound G.M., *J. Cryst. Growth*, 1974, vol. 23, pp. 45.
- [112] Morris J.R., Wang C.Z., Ho K.M., and Chan C.T., *Phys. Rev. B*, 1994, vol. 49, pp. 3109.
- [113] Morris J.R. and Song X., *J. Chem. Phys.*, 2002, vol. 116, pp. 9352.
- [114] Fensin S.J. et al. *Physical Review E*, 2010, vol. 81, pp. 031601.
- [115] Laird B.B. and Haymet A.D., *J. Chem. Rev.*, 1992, vol. 92, pp. 1819-1837.
- [116] Huitema H.E.A., Vlot M.J. and van de Eerden J.P., *J. Chem. Phys.*, September

1999, vol. 111, no. 10, pp. 8.

[117] Broughton J.Q. and Gilmer G.H., *J. Chem. Phys.*, 1986, vol. 84, pp. 5749.

[118] Davidchack R.L. and Laird B.B., *Molecular Physics*, 1999, vol. 97, no. 7, pp. 833-839.

[119] Ramalingam H., Asta M., van de Walle A. and Hoyt J.J., *Interface Science*, 2002, vol. 10, pp. 149–158.

[120] Buta D., Asta M. and Hoyt J.J., *Physical Review E*, 2008, vol. 78, pp. 031605.

[121] Sibug-Aga R., and Laird B.B., *Physical Review B*, 2002, vol. 66, pp. 144106.

[122] Hoyt J.J. et al., *Materials Science and Engineering R*, 2003, vol. 41, pp. 121–163.